NASA/TP—2005–214188

Baseline Computational Fluid Dynamics Methodology for Longitudinal-Mode Liquid-Propellant Rocket Combustion Instability

R.J. Litchford
Marshall Space Flight Center, Marshall Space Flight Center, Alabama

September 2005

The NASA STI Program Office…in Profile

Since its founding, NASA has been dedicated to the advancement of aeronautics and space science. The NASA Scientific and Technical Information (STI) Program Office plays a key part in helping NASA maintain this important role.

The NASA STI Program Office is operated by Langley Research Center, the lead center for NASA's scientific and technical information. The NASA STI Program Office provides access to the NASA STI Database, the largest collection of aeronautical and space science STI in the world. The Program Office is also NASA's institutional mechanism for disseminating the results of its research and development activities. These results are published by NASA in the NASA STI Report Series, which includes the following report types:

- TECHNICAL PUBLICATION. Reports of completed research or a major significant phase of research that present the results of NASA programs and include extensive data or theoretical analysis. Includes compilations of significant scientific and technical data and information deemed to be of continuing reference value. NASA's counterpart of peer-reviewed formal professional papers but has less stringent limitations on manuscript length and extent of graphic presentations.

- TECHNICAL MEMORANDUM. Scientific and technical findings that are preliminary or of specialized interest, e.g., quick release reports, working papers, and bibliographies that contain minimal annotation. Does not contain extensive analysis.

- CONTRACTOR REPORT. Scientific and technical findings by NASA-sponsored contractors and grantees.

- CONFERENCE PUBLICATION. Collected papers from scientific and technical conferences, symposia, seminars, or other meetings sponsored or cosponsored by NASA.

- SPECIAL PUBLICATION. Scientific, technical, or historical information from NASA programs, projects, and mission, often concerned with subjects having substantial public interest.

- TECHNICAL TRANSLATION. English-language translations of foreign scientific and technical material pertinent to NASA's mission.

Specialized services that complement the STI Program Office's diverse offerings include creating custom thesauri, building customized databases, organizing and publishing research results…even providing videos.

For more information about the NASA STI Program Office, see the following:

- Access the NASA STI Program Home Page at ***http://www.sti.nasa.gov***

- E-mail your question via the Internet to help@sti.nasa.gov

- Fax your question to the NASA Access Help Desk at 301–621–0134

- Telephone the NASA Access Help Desk at 301–621–0390

- Write to:
  NASA Access Help Desk
  NASA Center for AeroSpace Information
  7121 Standard Drive
  Hanover, MD 21076–1320
  301–621–0390

NASA/TP—2005–214188

Baseline Computational Fluid Dynamics Methodology for Longitudinal-Mode Liquid-Propellant Rocket Combustion Instability

R.J. Litchford
Marshall Space Flight Center, Marshall Space Flight Center, Alabama

National Aeronautics and
Space Administration

Marshall Space Flight Center • MSFC, Alabama 35812

September 2005

Available from:

NASA Center for AeroSpace Information
7121 Standard Drive
Hanover, MD 21076–1320
301–621–0390

National Technical Information Service
5285 Port Royal Road
Springfield, VA 22161
703–487–4650

TABLE OF CONTENTS

LIST OF FIGURES

LIST OF ACRONYMS AND SYMBOLS

2CD	second-order central difference
2UP	second-order upwind scheme
3UP	third-order biased upwind scheme
CFD	computational fluid dynamics
CN	Crank-Nicholson
EI	Euler implicit
PDF	probability density function
SMD	Sauter mean diameter
TVD	total-variation-diminishing

NOMENCLATURE

A	Jacobian coefficient matrix; cross-sectional area
A^+, A^-	Jacobian matrices for positive or negative eigenvalues
$\tilde{A}$	Roe-averaged Jacobian coefficient matrix
a	acoustic admittance based on mass flux
a_{sn}	short-nozzle acoustic admittance coefficient based on mass flux
B	instantaneous value of flow parameter at computational boundary
B^*	fixed value of flow parameter at computational boundary
C_0	streamline characteristic
C_+	right-running Reimann variable characteristic
C_-	left-running Reimann variable characteristic
C_D	drag coefficient, $= 24\left(1 + \mathrm{Re}^{2/3}/6\right)/\mathrm{Re}\ ;\ \mathrm{Re} < 1{,}000$
	$= 0.424\ ;\ \mathrm{Re} \geq 1{,}000$
C_p	constant-pressure specific heat
C_v	constant-volume specific heat
c	instantaneous acoustic velocity
$\bar{c}$	mean acoustic velocity
c'	perturbed acoustic velocity
D	interphase momentum exchange per unit volume, $= (\pi/8) n d_p^2 \rho C_D \left\lvert u_p - u \right\rvert \left(u_p - u\right)$
d_p	instantaneous Sauter diameter of propellant spray

NOMENCLATURE (Continued)

$\bar{d}_p$	mean Sauter diameter of propellant spray
d'_p	perturbed Sauter diameter of propellant spray
E	convective flux vector
$\tilde{E}$	numerical flux vector
$\hat{E}$	gradient limited flux vector
e	total internal energy
f	frequency of acoustic oscillations
H	source vector
H_1, H_2	source vector components related to area change and interphase transport
h	specific stagnation enthalpy
i	imaginary number, $= \sqrt{-1}$
j	numerical grid index
K_1, K_2	arbitrary constants
K_u	velocity sensitive propellant vaporization/combustion rate
K_p	pressure sensitive propellant vaporization/combustion rate
k	isentropic process invariant
L	characteristic selection matrix
l_a	atomization length
l_c	combustor length
l_d	duct length
M	conservative-to-primitive variable transformation matrix; Mach number
$\bar{M}_b$	mean transpiration Mach number at injector face boundary

NOMENCLATURE (Continued)

$\dot{m}_g$	local gaseous flow rate in combustor
$\dot{m}_p$	instantaneous vaporization/combustion rate of dispersed propellant
$\bar{\dot{m}}_p$	mean vaporization/combustion rate of dispersed propellant
$\dot{m}'_p$	perturbed vaporization/combustion rate of dispersed propellant
$\dot{m}_s$	instantaneous vaporization/combustion rate at injector face surface
$\bar{\dot{m}}_s$	mean vaporization/combustion rate at injector face surface
$\dot{m}'_s$	perturbed vaporization/combustion rate at injector face surface
$\dot{m}_{tot}$	total propellant injection rate
N_{grid}	number of grid points per wavelength of first longitudinal acoustic mode
N_λ	total number of grid points
n	propellant droplet number density, numerical time index; acoustic mode
P	period of oscillation
p	instantaneous pressure
$\bar{p}$	mean pressure
p'	pressure perturbation
p_{ex}	pressure at flow exit boundary (i.e., nozzle entrance plane)
Q	conserved variable vector
q_c	heat of combustion
q_v	heat of vaporization
R	ideal gas constant; residual explicit operator
S	cross-sectional area
s	instantaneous specific entropy

NOMENCLATURE (Continued)

$\bar{s}$	mean specific entropy
s'	perturbed specific entropy
T	temperature; similarity transformation matrix
$\bar{T}_b$	mean transpiration temperature at injector face boundary
T_{flame}	flame temperature
t	time
u	instantaneous gas velocity
$\bar{u}$	mean gas velocity
u'	perturbed gas velocity
u_p	liquid-propellant velocity
V	primitive variable vector
$\dot{w}$	propellant vaporization/combustion rate per unit volume
x	axial spatial coordinate
x_p	axial spatial position of propellant parcel
z	acoustic impedance
z_{in}	acoustic impedance at duct inlet boundary
z_{ex}	acoustic impedance at duct exit boundary
α_a	pressure sensitive response index for atomization
α_s	pressure sensitive response index for injector face surface combustion
α_v	pressure sensitive response index for dispersed propellant combustion
α_v^*	complex pressure sensitive index for dispersed propellant combustion
β	numerical compression parameter

NOMENCLATURE (Continued)

$\bar{\beta}$	mean burning rate constant for dispersed propellant
β_a	velocity-sensitive response index for atomization
β_s	velocity-sensitive response index for injector face surface combustion
β_v	velocity-sensitive response index for dispersed propellant combustion
β_v^*	complex velocity-sensitive index for dispersed propellant combustion
γ	specific heat ratio
Δ	discretization operator
θ	temporal discretization selection parameter
κ	spatial discretization selection parameter
Λ	diagonal eigenvalue matrix
Λ^+, Λ^-	positive/negative components of diagonal eigenvalue matrices
λ	acoustic amplification coefficient
μ	complex acoustic wave number
μ_1, μ_1	characteristic acoustic wave numbers
ρ	gas density
ρ_p	liquid-propellant density
τ	relaxation time, $= (4/3)(\rho_p/\rho)(d_p/C_D)\lvert u_p - u\rvert^{-1}$
τ_α	pressure-sensitive phase lag for dispersed propellant combustion
τ_β	velocity-sensitive phase lag for dispersed propellant combustion
Ω	complex acoustic frequency
ω	radial frequency of acoustic oscillations

TECHNICAL PUBLICATION

BASELINE COMPUTATIONAL FLUID DYNAMICS METHODOLOGY FOR LONGITUDINAL-MODE LIQUID-PROPELLANT ROCKET COMBUSTION INSTABILITY

1. INTRODUCTION

Liquid-propellant rocket combustion instability research has been pursued with varying degrees of emphasis for more than 50 yr. These efforts have led to the successful development of many reliable engines, which have been mainly the result of much trial and error development testing based on a great deal of intuition and experience, and engine design remains today as much engineering art as science. A detailed understanding of the mechanism by which combustion instability occurs in these devices simply does not exist, and the occurrence of resonant combustion instabilities continues to be a major risk in the development of any new liquid-propellant rocket engine.

Previous predictive methods have been based primarily on approximate analytical models, but computational fluid dynamics (CFD) capability has advanced to the stage where it can now be effectively used as a research and development tool.[1] Clearly, CFD methods have the potential to resolve the fundamental chamber processes in great physical detail, yet these results are highly dependent on the validity and fidelity of the various physical submodels. For this reason, CFD, at this stage, is more valuable as a computational test-bed than as a practical design tool.

Utilization of CFD methods for the combustion instability problem also requires careful consideration of numerical accuracy. For example, both the dissipative and dispersive characteristics of a particular scheme can have an important influence on numerical accuracy in unsteady flow problems, as demonstrated by Hsieh.[2] Furthermore, stability limits can be greatly affected by the transmission and reflection of flow disturbance incident on the boundaries, and implementation of appropriate boundary conditions is not trivial.

This Technical Publication develops and evaluates a computational method for the analysis of longitudinal-mode liquid-propellant rocket combustion instability based on the unsteady, quasi-one-dimensional Euler equations. The unsteady Euler equations in inhomogeneous form retain full hyperbolicity and are integrated implicitly in time using a second-order, high-resolution, characteristic-based, flux-differencing spatial discretization with Roe averaging of the Jacobian matrix. Combustion process source terms were introduced through the incorporation of a two-zone, linearized representation: (1) A two-parameter collapsed combustion zone at the injector face, or (2) a two-parameter distributed combustion zone in which interphase transport is derived from a Lagrangian treatment of the propellant spray. The method is evaluated against a simplified analytical solution based on linearized small disturbance theory, and the numerical methodology is then exercised on a generic combustor configuration

using both collapsed and distributed combustion zone models with a short-nozzle admittance approximation for the outflow boundary.

The resulting baseline open-source CFD code is able to serve educational/pedagogical needs in its current form and could eventually be developed into a practical research and development tool by extending the methodology to multiple dimensions, incorporating realistic physical submodels, and engaging in a painstaking validation effort. Ultimately, CFD methods may be of most practical utility as computational test-beds for investigating and studying the underlying physico-chemical mechanisms associated with liquid-propellant rocket combustion instability.

2. THEORETICAL AND MATHEMATICAL FORMULATION

2.1 Governing Equations

The gas phase is treated using an Eulerian description with appropriate source terms for interphase transport coupling with the spray. Thus, the problem reduces to solving the unsteady, quasi-one-dimensional Euler equations, which may be written in conservative form using matrix notation as

$$\frac{\partial Q}{\partial t} + \frac{\partial E}{\partial x} = H \quad , \tag{1}$$

where the conserved variable vector, Q, and the convective flux vector, E, are defined by

$$Q = \begin{bmatrix} \rho S \\ \rho u S \\ \rho e S \end{bmatrix} \tag{2}$$

and

$$E = \begin{bmatrix} \rho u S \\ \left(\rho u^2 + p\right) S \\ \left(\rho u e + u p\right) S \end{bmatrix} . \tag{3}$$

The source vector, H, contains contributions due to the variable cross-section area and interphase transport source terms. This vector is denoted as the sum of two components:

$$H = H_1 + H_2 \quad . \tag{4}$$

For single-phase flow, only H_1 need be considered to account for the variable area effect on the momentum equation. It consists of a single component:

$$H_1 = \begin{bmatrix} 0 \\ p \dfrac{\partial S}{\partial x} \\ 0 \end{bmatrix} . \tag{5}$$

For two-phase flow, the source vector H_2 must be included to account for interphase transport effects on the gas-phase conservation equation. It has the form

$$H_2 = \begin{bmatrix} S\dot{w} \\ S\dot{w}u_p + D \\ S\dot{w}\left\{\left(q_c - q_v\right) + u_p^2/2\right\} + SuD \end{bmatrix} . \tag{6}$$

Here, $\dot{w}$ represents the propellant vaporization/combustion rate per unit volume. The perfect gas equation of state $p = \rho RT = (\gamma - 1)\left[e - \rho u^2/2\right]$ completes the governing system, where $e = C_v T + u^2/2$ represents the total internal energy.

This inhomogeneous form of the Euler equations retains full hyperbolicity. Thus, the Jacobian coefficient matrix, $A = \partial E/\partial Q$, has real eigenvalues ($u$, $u + c$, and $u - c$ with the speed of sound defined by $c = \sqrt{\gamma p/\rho}$). Following conventional practice, A may be diagonalized such that

$$T^{-1}M^{-1}AMT = \Lambda \ , \tag{7}$$

where $M = \partial Q/\partial V$ is a transformation matrix from the conservation variables Q to the primitive variables V, T is a similarity transformation matrix formed from the eigenvectors of the primitive variable Jacobian coefficient matrix $M^{-1}AM$, and $\Lambda = \text{ diag } \{u, u + c, u - c\}$ is the diagonal eigenvalue matrix.

For convenience, positive and negative eigenvalue matrices may be defined as $\Lambda^{\pm}$, where Λ^{+} contains only positive eigenvalues and Λ^{-} contains only negative eigenvalues. It therefore follows that $A = MT\left(\Lambda^{+} + \Lambda^{-}\right)T^{-1}M^{-1} = A^{+} + A^{-}$ and $|A| = MT\left(\Lambda^{+} - \Lambda^{-}\right)T^{-1}M^{-1} = A^{+} - A^{-}$.

2.2 Numerical Scheme

Integration of the Euler equations is accomplished through temporal and spatial finite-difference discretization with appropriate linearization. For spatial discretization, a conservative formulation was desired that could yield good spatial resolution while avoiding spurious numerical oscillations. In selecting a time-integration method, the central concerns were obtaining adequate time-accuracy and good numerical stability. These attributes are central to the description of unsteady flows typically encountered in a combustion stability analysis. Therefore, both the dissipative and dispersive characteristics of a numerical scheme are important points of consideration.

An assessment of numerical techniques for unsteady flow calculations has been carried out by Hsieh.[2] Based on his survey of various spatial discretization schemes, sixth-order central differencing of the convective fluxes and fourth-order artificial dissipation yielded very good all around performance. He also explored characteristic-based schemes and found that second-order upwind scheme (2UP) flux differencing using Roe-averaged Jacobian coefficient matrices and nonlinear flux limiters to achieve total-variation-diminishing (TVD) conditions performed very well with regard to shock capturing but entailed higher dissipative errors in multidimensional problems. This characteristic based spatial discretization scheme was adopted, along with a generalized implicit time integration method, for the present development. Although not quite as effective as an explicit Runge-Kutta multistage approach, implicit time integration provides adequate resolution and stability and is very robust.

2.2.1 Discretization

Development of the numerical scheme begins with a generalized implicit formulation for the Euler equations in the form

$$\Delta Q_j^n + \theta\left[\frac{\Delta t}{\Delta x}\left(\tilde{E}_{j+1/2} - \tilde{E}_{j-1/2}\right) - \Delta t H_j\right]^{n+1} + (1-\theta)\left[\frac{\Delta t}{\Delta x}\left(\tilde{E}_{j+1/2} - \tilde{E}_{j-1/2}\right) - \Delta t H_j\right]^{n} = 0 \ , \qquad (8)$$

where $\theta = 1$ yields the Euler implicit (EI) scheme and $\theta = 1/2$ yields the Crank-Nicholson (CN) (trapezoidal) scheme. The first term is defined by $\Delta Q_j^n = Q_j^{n+1} - Q_j^n$, and the numerical flux, $\tilde{E}$, is detailed to first-order accuracy by

$$\tilde{E}_{j+1/2}^{(1)} = \frac{1}{2}\left[E_j + E_{j+1} - \left|\tilde{A}\right|_{j+1/2}\left(Q_{j+1} - Q_j\right)\right] \ . \qquad (9)$$

where $\tilde{A}$ is the Jacobian coefficient matrix evaluated using the Roe-averaged quantities[3,4]

$$\rho_{j+1/2} = \sqrt{\rho_{j+1}\rho_j} \ , \qquad (10)$$

$$u_{j+1/2} = \frac{u_j\sqrt{\rho_j} + u_{j+1}\sqrt{\rho_{j+1}}}{\sqrt{\rho_j} + \sqrt{\rho_{j+1}}} \ , \qquad (11)$$

$$h_{j+1/2} = \frac{h_j\sqrt{\rho_j} + h_{j+1}\sqrt{\rho_{j+1}}}{\sqrt{\rho_j} + \sqrt{\rho_{j+1}}} \ , \qquad (12)$$

and

$$c_{j+1/2} = \sqrt{(\gamma-1)\left[h_{j+1/2} - \frac{u_{j+1/2}^2}{2}\right]} \ . \qquad (13)$$

The delta form of the generalized implicit scheme is obtained by introducing $\Delta\tilde{E}^n = \tilde{E}^{n+1} - \tilde{E}^n$ and $\Delta H^n = H^{n+1} - H^n = \partial H/\partial Q\,\Delta Q^n$:

$$\Delta Q_j^n + \theta\left[\frac{\Delta t}{\Delta x}\left(\Delta\tilde{E}_{j+1/2}^n - \Delta\tilde{E}_{j-1/2}^n\right) - \Delta t\left.\frac{\partial H}{\partial Q}\right|_j \Delta Q_j^n\right] = -R\left(Q_j^n\right) \ , \qquad (14)$$

where

$$\Delta\tilde{E}^n_{j+1/2} = \frac{1}{2}\left[\Delta E_j + \Delta E_{j+1} - \left|\tilde{A}\right|_{j+1/2}\left(\Delta Q_{j+1} - \Delta Q_j\right)\right]^n \tag{15}$$

and $R\left(Q^n_j\right)$ is a residual explicit operator defined by

$$R\left(Q^n_j\right) = \frac{\Delta t}{\Delta x}\left(\tilde{E}^n_{j+1/2} - \tilde{E}^n_{j-1/2}\right) - \Delta t H^n_j \quad . \tag{16}$$

The variable cross-sectional area effect is included in the source vector Jacobian, but all interphase transport appears in the residual explicit operator. To arrive at the final form used for computation, substitute $\Delta E_j = A_j \Delta Q_j$ and collect like terms to yield

$$\begin{aligned}
&\left\{-\theta\frac{\Delta t}{2\Delta x}\left(A^n_{j-1} + \left|\tilde{A}\right|^n_{j-1/2}\right)\right\}\Delta Q^n_{j-1} \\
&\qquad + \left\{I - \theta\Delta t\left.\frac{\partial H}{\partial Q}\right|_j + \theta\frac{\Delta t}{2\Delta x}\left(\left|\tilde{A}\right|^n_{j+1/2} + \left|\tilde{A}\right|^n_{j-1/2}\right)\Delta Q^n_j\right\} \\
&\qquad + \left\{\theta\frac{\Delta t}{2\Delta x}\left(A^n_{j+1} + \left|\tilde{A}\right|^n_{j+1/2}\right)\right\}\Delta Q^n_{j+1} \quad .
\end{aligned} \tag{17}$$

This first-order accurate scheme exhibits robust nonoscillatory behavior, but spatial resolution is poor. Direct substitution of second-order difference formulas does not improve matters either because this leads to the generation of spurious oscillations. To circumvent this difficulty, Harten has introduced the TVD property and derived sufficient conditions for constructing schemes that satisfy this property.[5] Such constructions have been carried out for both explicit and implicit time integration schemes.[6,7] The mechanisms currently in use for TVD conditions are based on some kind of gradient limiting procedure. We adapt the procedure based on a nonlinear flux limiter. The second-order convective flux vector is obtained by adding corrective terms to the first-order flux vector. A generalized form which may be specialized for second-order central difference (2CD), 2UP, or third-order biased upwind scheme (3UP) is given by[2]

$$\tilde{E}^{(2)}_{j+1/2} = \tilde{E}^{(1)}_{j+1/2} + \frac{1-\kappa}{4}\left[\Delta\hat{E}^+_{j-1/2} - \Delta\hat{E}^-_{j+3/2}\right] + \frac{1+\kappa}{4}\left[\Delta\hat{E}^+_{j+1/2} - \Delta\hat{E}^-_{j+1/2}\right] , \tag{18}$$

where

$$\Delta\hat{E}^-_{j+1/2} = \left(MT\right)_{j+1/2}\Delta\hat{\sigma}^-_{j+1/2} \quad , \tag{19}$$

$$\Delta\hat{E}^+_{j+1/2} = \left(MT\right)_{j+1/2}\Delta\hat{\sigma}^+_{j+1/2} \quad , \tag{20}$$

$$\Delta\hat{\sigma}^-_{j+1/2} = \min\mathrm{mod}\left[\Delta\sigma^-_{j+1/2}, \beta\Delta\sigma^-_{j-1/2}\right] , \tag{21}$$

$$\Delta\hat{\sigma}^{+}_{j+1/2} = \min\mathrm{mod}\left[\Delta\sigma^{+}_{j+1/2}, \beta\Delta\sigma^{+}_{j-3/2}\right] , \tag{22}$$

$$\Delta\sigma^{-}_{j+1/2} = \frac{1}{2}\left(\Lambda - |\Lambda|\right)_{j+1/2}\left(T^{-1}M^{-1}\right)_{j+1/2}\left(Q_{j+1} - Q_j\right) , \tag{23}$$

$$\Delta\sigma^{+}_{j+1/2} = \frac{1}{2}\left(\Lambda + |\Lambda|\right)_{j+1/2}\left(T^{-1}M^{-1}\right)_{j+1/2}\left(Q_{j+1} - Q_j\right) , \tag{24}$$

and the minmod operator is defined by

$$\min\mathrm{mod}[x, y] = \mathrm{sgn}(x)\max\left[0, \min\left\{|x|, y\,\mathrm{sgn}(x)\right\}\right] . \tag{25}$$

The values of κ corresponding to the alternative spatial discretization schemes are $\kappa = 1$ for 2CD, $\kappa = -1$ for 2UP, and $\kappa = 1/3$ for 3UP.

The constant, β, is a compression parameter that is restricted to the range $1 \le \beta \le (3-\kappa)/(1-\kappa)$ with $\beta = 6$ when $\kappa = 1$. To maintain an efficient algorithm, some time accuracy is sacrificed by including the second-order numerical flux in the residual explicit operator only. In this way, the tridiagonal block structure of the first-order flux is maintained; thereby, avoiding a pentadiagonal block system.

2.2.2 Boundary Conditions

Boundary conditions for the computational analysis are implemented according to the propagation of information along the flow characteristics. On a locally one-dimensional basis, for instance, each eigenvalue may be associated with a particular characteristic. If the eigenvalue is positive, the corresponding characteristic is right running. Conversely, if the eigenvalue is negative, the characteristic is left running. When a characteristic runs out of the computational domain, the boundary condition depends on the internal flow field, and a numerical boundary condition must be formulated that depends on the computed solution. The number of unknown flow parameters minus the number of numerical boundary conditions gives the number of physical boundary conditions that must be imposed. The numerical and physical boundary conditions must be compatible with the system of equations for the characteristic variables.

The numerical boundary conditions are formulated for an implicit scheme from the characteristic form of the equations with a selection matrix for choosing the outgoing characteristics. Also, one-sided differences are used to couple a boundary node to the interior. The resulting forms are as follows:

Inflow boundary $(j = 1)$:

$$L\left(T^{-1}M^{-1}\right)\left[\Delta Q^{n}_{j} + \theta\frac{\Delta t}{\Delta x/2}\Delta\tilde{E}^{n}_{j+1/2} - \Delta t\left.\frac{\partial H}{\partial Q}\right|_{j}\Delta Q_j\right] = -L\left(T^{-1}M^{-1}\right)R\left(Q^{n}_{j}\right) . \tag{26}$$

Outflow boundary $(j = J)$:

$$L\left(T^{-1}M^{-1}\right)\left[\Delta Q_j^n + \theta\frac{\Delta t}{\Delta x/2}\Delta\tilde{E}_{j-1/2}^n - \Delta t\left.\frac{\partial H}{\partial Q}\right|_j \Delta Q_j\right] = -L\left(T^{-1}M^{-1}\right)R\left(Q_j^n\right) \quad . \tag{27}$$

Here, $T^{-1}M^{-1}$ is introduced to obtain the characteristic variables and L is the characteristic selection matrix. For example, to choose the left-running characteristic only for subsonic inflow, $L = \text{diag}\ \{0,0,1\}$. In the case of supersonic outflow, there are three outrunning characteristics such that $L = \text{diag}\ \{1,1,1\}$. If the outflow boundary is subsonic, on the other hand, there are only two right-running characteristics, and $L = \text{diag}\ \{1,1,0\}$. By using one-sided differences, each numerical boundary relation has a two-node support involving a boundary node and an adjacent interior node.

The imposed physical boundary conditions are imposed by letting B^* represent the specified boundary flow parameter. Then, Newton iteration implies $B^{n+1} = B^n + \partial B/\partial Q\,\Delta Q^n$, and by enforcing $B^{n+1} \to B^*$, we obtain the constraining relationship

$$\left.\frac{\partial B}{\partial Q}\right|_j \Delta Q_j^n = B^* - B^n \quad . \tag{28}$$

Both the linearized numerical and physical boundary relations are solved with the system of linear algebraic equations for the interior nodes.

2.3 Combustion Model

A generalized schematic of a conventional liquid propellant rocket engine is shown in figure 1. Propellant combustion in the rocket chamber is modeled as a two-zone process consisting of a collapsed combustion zone at the injector face boundary and a distributed combustion zone extending from the injector face to the point where propellant reaction is completed. Thus, the inflow boundary for the computation is a transpiring reactive surface in which a small fraction of the propellant enters as a hot subsonic gaseous flow while the bulk of the propellant enters in the form of an unreacted liquid spray. Thus, the subsonic inflow boundary has only one outrunning characteristic, and two physical boundary conditions must be specified.

The propellant combustion rate can be sensitive to pressure and velocity fluctuations, which permits the development of a feedback loop for combustion-driven instabilities. Here, simplified two-parameter linear formulations are introduced to account for these sensitivities in both the collapsed and distributed combustion models. Furthermore, a two-parameter linearized spray atomization model has also been incorporated to reflect similar sensitivities associated with this process. The computational domain and the various submodel regions are illustrated in figure 2.

2.3.1 Collapsed Combustion Zone

Imposing a collapsed combustion zone at the injector face provides a mechanism for burned gaseous propellant to enter the computational domain at the inflow boundary. Thus, from a physical perspective, the inflow boundary may be viewed as a transpiring reactive boundary layer. Here, the characteristics

of this transpiring reactive boundary may be defined by the mean burned gas Mach number, $\bar{M}_b$, and the mean burned gas temperature, $\bar{T}_b$. For convenience, we express the injector face combustion source as the sum of a steady mean flow quantity and an unsteady perturbation:

$$\dot{m}_s = \bar{\dot{m}}_s + \dot{m}'_s \quad , \tag{29}$$

where the mean mass transpiration rate corresponds to the steady solution for the particular rocket engine under consideration.

Sensitivity of the transpiring combustion rate to pressure fluctuations and the time rate of change in these pressure fluctuations is accounted for through a simple phenomenological two-parameter linearized model in the form[8]

$$\frac{\dot{m}'_s}{\bar{\dot{m}}_s} = \alpha_s \frac{p'}{\bar{p}} + \beta_s \left(\frac{l_c}{\bar{p}\bar{c}} \right) \frac{\partial p'}{\partial t} \quad , \tag{30}$$

where the overbars symbolize mean quantities and primes represent perturbations. The second term on the right-hand side introduces a characteristic time scale defined as the ratio of the combustor length, l_c, to the mean acoustic velocity, $\bar{c}$.

2.3.2 Atomization Zone

The remainder of the propellant not consumed in the collapsed combustion zone is assumed to enter the computational domain in the form of liquid jets that completely atomize over a predefined length, l_a. The resulting spray is characterized by a Sauter mean diameter (SMD), which is then used to compute the effective interphase transport terms. Because the atomization process is sensitive to both pressure and velocity fluctuations, the SMD can actually display a time-dependent variation that is directly coupled to chamber oscillations. To capture the underlying fundamental coupling process, a linearized two-parameter atomization model is adapted using the form

$$\frac{d'_p}{\bar{d}_p} = \alpha_a \frac{p'}{\bar{p}} + \beta_a \frac{u'}{\bar{u}} \quad , \tag{31}$$

where α_a is the pressure sensitive index and β_a is the velocity sensitive index for atomization. Numerical values for these parameters have been derived for various atomization models and are tabulated by Grenda et al.[9]

2.3.3 Distributed Combustion Zone

The atomized propellant spray is represented as a collection of discrete computational parcels which are injected into the combustor at specified time intervals. Each parcel is identified with a group of physical droplets, the number of which is determined from the propellant injection rate and the mean droplet size. The spatial distribution of the physical particles within each computational parcel is defined by a

probability density function (PDF) in space. The behavior of the physical droplets is determined by the history of their representative parcel, whose position corresponds to the mean of the PDF. The parcels are tracked through the combustor using a Lagrangian procedure, and knowledge of the shape and statistical parameters of the PDF permits calculation of interphase transport terms.

PDF representation is utilized in order to minimize the numerical shot noise that can result when each parcel is described by a delta function point source and the ratio of parcels to physical droplets in the spray is too small. The numerical noise arising from a point source distribution function can be minimized by using a large number of parcels; however, such an approach can be extremely costly in terms of computational efficiency.

Here, we employ a rectangular uniform PDF shape that is fully defined given the mean position and half-width. The streamwise width of the PDF corresponds to the product of the injection velocity and a specified injection time interval, which is generally set to obtain a PDF width on the order of the computational cell width. In addition, the PDF shape and width remain fixed throughout a parcel's lifetime.

The mean position of each PDF is determined from the Lagrangian tracking of a single computational parcel characterizing the behavior of the physical droplets in the group. Thus, parcel motion is governed by the the equations of motion,

$$\frac{du_p}{dt} = \frac{3}{4}\frac{\rho_g}{\rho_p}\frac{C_D}{d_p}\left|u - u_p\right|\left(u - u_p\right) \tag{32}$$

and

$$\frac{dx_p}{dt} = u_p \quad . \tag{33}$$

For the sake of simplicity, these equations are linearized by holding $\left(\rho_g/\rho_p\right)\left(C_D/d_p\right)\left|u - u_p\right|$ constant over the computational time step and integrating analytically. This gives the updated parcel velocity as

$$u_p \approx u_{p,0}\exp\left[\frac{-\Delta t}{\tau}\right] + u\left\{1 - \exp\left[\frac{-\Delta t}{\tau}\right]\right\} \tag{34}$$

and the parcel position is obtained using explicit Euler integration

$$x_p \approx x_{p,0} + u_{p,0}\Delta t \quad . \tag{35}$$

The unsteady combustion rate for each parcel is assumed to be governed by the vaporization rate, which can be linearized about some mean steady state to obtain a vaporization-controlled combustion response function. For convenience, we express the local propellant combustion rate as the sum of a steady mean flow quantity and an unsteady perturbation:

$$\dot{m}_p = \bar{\dot{m}}_p + \dot{m}'_p \quad , \tag{36}$$

where the instantaneous vaporization/combustion rate has the general form

$$\dot{m}_p = \bar{\dot{m}}_p \left(K_p + K_u \right) \tag{37}$$

and K_p and K_u represent the pressure and velocity sensitivities, respectively. The mean mass burning rate of a parcel is governed by the mean burning rate constant, $\bar{\beta}$, such that

$$\bar{\dot{m}}_p = \frac{\pi}{4} \rho_p d_p \bar{\beta} \ . \tag{38}$$

Note that the evaluation of the instantaneous propellant vaporization/combustion rate requires knowledge of the droplet temperature variation with time. The simplest feasible model for internal energy transport that can account for local gas-dynamic fluctuations is based on the rapid-mixing limit assumption. Here, the droplet temperature is assumed to be uniform due to strong internal circulation, but its time rate of change is allowed to vary according to the balance between the energy leaving the surface due to vaporization and the energy arriving due to heat transfer. Linearization of this model leads to a parcel combustion response function of the form:[9]

$$\frac{\dot{m}'_p}{\bar{\dot{m}}_p} = \alpha_v^* \frac{p'}{\bar{p}} + \beta_v^* \frac{u'}{\bar{u}} \ , \tag{39}$$

where the pressure- and velocity-sensitive indices, α_v^* and β_v^*, are complex coefficients due to the phase difference that can exist between the vaporization and gas oscillations as a result of temporal oscillations inside the droplet. This phase difference can also be accounted for through the introduction of appropriate time lags when evaluating the fluctuating gas-dynamic properties such that the response indices are real numbers

$$\frac{\dot{m}'_p}{\bar{\dot{m}}_p} = \alpha_v \frac{p'\left(t - \tau_\alpha\right)}{\bar{p}} + \beta_v \frac{u'\left(t - \tau_\beta\right)}{\bar{u}} \ . \tag{40}$$

These combustion response time lags can have important effects on combustor stability and, in general, may not be neglected.

2.4 Short-Nozzle Approximation

In general, the computation should proceed through the converging-diverging section to the nozzle exit. Here, the flow is supersonic, and all of the characteristics are outrunning so that no physical conditions need be specified. However, it is often sufficient to employ a subsonic outflow boundary condition at the nozzle entrance by making the well-known short-nozzle approximation.[10,11] That is, the flow is assumed to accelerate to sonic velocity in zero length, which is equivalent to fixing the Mach number at the subsonic outflow boundary, $M' = 0$, for the single in-running characteristic. This approximation is strictly valid for pure longitudinal-mode oscillations only and, at worst, underestimates the nozzle damping effect. To obtain a mean flow solution prior to making a combustor stability calculation, it is necessary to specify the static pressure at the nozzle entrance such that it matches the mean chamber pressure for the rocket engine.

The short-nozzle approximation can also be expressed in terms of an admittance relationship in the form

$$\left.\frac{\rho u'}{\overline{\rho}\,\overline{u}}\right|_e = a_{sn}\left.\frac{p'}{\overline{p}}\right|_e \quad , \tag{41}$$

where a_{sn} is the short-nozzle admittance coefficient. It is of interest to derive an expression for this admittance coefficient using small disturbance linearization theory.

First, note that equation (41) is equivalent to the differential form

$$a_{sn}\frac{dp}{p} = \frac{\rho du + u d\rho}{\rho u} = \frac{du}{u} + \frac{d\rho}{\rho} \quad . \tag{42}$$

Then, consider the Mach number definition, $M = u/c$, the isentropic relationship for an ideal gas, $p/\rho^{\gamma} = k$, and the acoustic velocity relationship for an ideal gas, $c = \sqrt{\gamma p/\rho}$. Taking the logarithm of these expressions and putting them in differential form yields

$$\frac{dc}{c} = \frac{du}{u}\,;\ \frac{dp}{p} = \gamma\frac{d\rho}{\rho}\,;\ \frac{dc}{c} = \frac{1}{2}\left[\frac{dp}{p} - \frac{d\rho}{\rho}\right] , \tag{43}$$

where the short-nozzle condition, $dM = 0$, has been enforced. Using these relationships to eliminate du/u and $d\rho/\rho$ in equation (42), we deduce the following value for the short-nozzle admittance coefficient:

$$a_{sn} = \frac{\gamma + 1}{2\gamma} \quad . \tag{44}$$

3. VALIDATION

As a baseline validation, it is convenient to examine the simplified case of unsteady, nonreacting, isentropic duct flow and to compare the numerical scheme predictions with small disturbance linear acoustics theory. In this way, the fidelity of the numerical scheme can be evaluated with respect to the basic underlying fluid dynamic phenomena in unsteady flow. Quantitative assessment of acoustic wave driving/damping mechanisms associated with chemical reaction processes is critically sensitive to the detailed physical submodeling and is ultimately dependent on empirical validation. Identification and verification of these driving and damping mechanisms are, of course, the central objectives of combustion instability research.

3.1 Linearized Small Perturbation Acoustics

For constant area duct flow, the continuity and momentum perturbation equations for an inviscid fluid may be combined to obtain an acoustic wave equation in the form[12]

$$\left(1-\bar{M}^2\right)\frac{\partial^2 p'}{\partial x^2}-\frac{1}{\bar{c}}\frac{\partial^2 p'}{\partial t^2}-\frac{2\bar{M}}{\bar{c}}\frac{\partial^2 p'}{\partial x \partial t}=0 \quad , \tag{45}$$

where the usual linearization definitions apply. Note that the cross derivative term in equation (45) arises as a consequence of the nonzero mean flow velocity, $\bar{u} \neq 0$, in the duct. Considering a complex harmonic solution of the form $p' \propto e^{i\mu x} e^{i\Omega t}$ in equation (45), we obtain the dispersion relationship

$$\left(1-\bar{M}^2\right)\mu^2-\frac{2\bar{M}}{\bar{c}}\Omega\mu-\frac{\Omega^2}{\bar{c}^2}=0 \quad , \tag{46}$$

which is quadratic in terms of the wave number μ. Thus, the characteristic wave numbers are

$$\mu_1=\frac{\Omega}{\left(1-\bar{M}\right)\bar{c}}\,;\;\; \mu_2=\frac{-\Omega}{\left(1+\bar{M}\right)\bar{c}} \quad , \tag{47}$$

and the complex harmonic solution takes the general form

$$\frac{p'}{\bar{p}}=K_1\left(e^{i\mu_1 x}+K_2 e^{i\mu_2 x}\right)e^{i\Omega t} \quad , \tag{48}$$

where K_1 and K_2 are undetermined constants.

Additional constraints follow from a consideration of the characteristic form of the Euler equations:[13]

$$\frac{\partial s}{\partial t} + u\frac{\partial s}{\partial x} = 0 \ , \tag{49}$$

$$\frac{\partial}{\partial t}\left(u + \frac{2}{\gamma - 1}c \right) + (u + c)\frac{\partial}{\partial x}\left(u + \frac{2}{\gamma - 1}c \right) = 0 \ , \tag{50}$$

and

$$\frac{\partial}{\partial t}\left(u - \frac{2}{\gamma - 1}c \right) + (u - c)\frac{\partial}{\partial x}\left(u - \frac{2}{\gamma - 1}c \right) = 0 \ , \tag{51}$$

which express the propagation of entropy along the streamline C_0 as defined by $dx/dt = u$ and the propagation of pressure waves, as described by the Riemann variables $w_2 = u + 2c/(\gamma - 1)$ and $w_3 = u - 2c/(\gamma - 1)$, along the characteristics C_+ and C_-, as defined by $dx/dt = u + c$ and $dx/dt = u - c$, respectively. For instance, linearization of the entropy conservation relationship about the mean value implies $s' \equiv 0$ (in the absence of flow discontinuities), and linearization of the Riemann characteristic equations yields

$$\frac{\partial}{\partial t}\left(u' + \frac{2}{\gamma - 1}c' \right) + \left[(\bar{u} + u') + (\bar{c} + c') \right]\frac{\partial}{\partial x}\left(u' + \frac{2}{\gamma - 1}c' \right) = 0 \tag{52}$$

and

$$\frac{\partial}{\partial t}\left(u' - \frac{2}{\gamma - 1}c' \right) + \left[(\bar{u} + u') - (\bar{c} + c') \right]\frac{\partial}{\partial x}\left(u' - \frac{2}{\gamma - 1}c' \right) = 0 \ , \tag{53}$$

from which complex harmonic solutions may be deduced:

$$\frac{u'}{\bar{u}} = -\frac{K_1}{\gamma \bar{M}}\left(e^{i\mu_1 x} - K_2 e^{i\mu_2 x} \right) e^{i\Omega t} \tag{54}$$

and

$$\frac{c'}{\bar{c}} = \frac{K_1(\gamma - 1)}{2\gamma}\left(e^{i\mu_1 x} + K_2 e^{i\mu_2 x} \right) e^{i\Omega t} \ . \tag{55}$$

In order to facilitate further development of the generalized solutions, it is useful to introduce the acoustic impedance function z as a parameter using the standard definition

$$\frac{p'}{\bar{p}} = z\frac{u'}{\bar{u}} \ . \tag{56}$$

Application of this impedance condition at the duct inlet implies $\left(p'/\bar{p}\right)/\left(u'/\bar{u}\right)\Big|_{x=0} = z_{in}$, and substitution of the complex harmonic solutions yields the result

$$K_2 = \frac{-\gamma\bar{M} - z_{in}}{\gamma\bar{M} - z_{in}} \ . \tag{57}$$

The impedance condition may also be applied at the duct exit to obtain $\left(p'/\bar{p}\right)/\left(u'/\bar{u}\right)\Big|_{x=l_d} = z_{ex}$, where substitution of the complex harmonic solutions gives the additional relation,

$$e^{i(\mu_2-\mu_1)\,l_d} = \frac{-\gamma\bar{M} - z_{ex}}{\gamma\bar{M} - z_{ex}}\frac{1}{K_2} \ . \tag{58}$$

Thus, equations (57) and (58) may be combined to obtain a relation between the characteristic wave numbers and the inlet/outlet acoustical impedances

$$e^{i(\mu_2-\mu_1)\,l_d} = \left(\frac{\gamma\bar{M} + z_{ex}}{\gamma\bar{M} - z_{ex}}\right)\left(\frac{\gamma\bar{M} - z_{in}}{\gamma\bar{M} + z_{in}}\right) \ . \tag{59}$$

Taking the natural logarithm of this equation yields the more convenient form

$$i\left(\mu_2 - \mu_1\right)\, l_d = \ln\left[\left(\frac{\gamma\bar{M} + z_{ex}}{\gamma\bar{M} - z_{ex}}\right)\left(\frac{\gamma\bar{M} - z_{in}}{\gamma\bar{M} + z_{in}}\right)\right] - i2n\pi \ , \tag{60}$$

and by noting that $\mu_2 - \mu_1 = -2\Omega\bar{c}/1-\bar{M}^2$, it is possible to develop a generalized relationship for Ω:

$$\Omega = \frac{\bar{c}\left(1-\bar{M}^2\right)}{2l_d}\left\{i\ln\left[\left(\frac{\gamma\bar{M} + z_{ex}}{\gamma\bar{M} - z_{ex}}\right)\left(\frac{\gamma\bar{M} - z_{in}}{\gamma\bar{M} + z_{in}}\right)\right] + 2n\pi\right\} \ . \tag{61}$$

Now, recall that the complex harmonic solution for acoustical disturbances at any fixed location in the duct is proportional to $e^{i\Omega t} = e^{\lambda t}e^{i\omega t}$, where an amplification coefficient, λ, and oscillation frequency, ω, have been defined such that

$$i\Omega = \lambda + i\omega = \frac{\bar{c}\left(\bar{M}^2 - 1\right)}{2l_d}\ln\left[\left(\frac{\gamma\bar{M} + z_{ex}}{\gamma\bar{M} - z_{ex}}\right)\left(\frac{\gamma\bar{M} - z_{in}}{\gamma\bar{M} + z_{in}}\right)\right] + i\frac{\bar{c}\left(1-\bar{M}^2\right)}{l_d}n\pi \ . \tag{62}$$

Thus, the amplification coefficient for acoustical disturbances in the duct is defined by the generalized expression

$$\lambda = \frac{\bar{c}\left(\bar{M}^2 - 1\right)}{2l_d}\ln\left[\left(\frac{\gamma\bar{M} + z_{ex}}{\gamma\bar{M} - z_{ex}}\right)\left(\frac{\gamma\bar{M} - z_{in}}{\gamma\bar{M} + z_{in}}\right)\right] \ , \tag{63}$$

and the period of oscillation, P, for a given acoustical mode, n, is given by

$$P = \frac{1}{f} = \frac{2\pi}{\omega} = \frac{2l_d}{n\bar{c}\left(1-\bar{M}^2\right)} \ . \tag{64}$$

Note that the value of the amplification coefficient governing acoustical growth/decay rates is dependent on the impedance functions for the duct inlet and exit. These parameters are determined from the application of appropriate boundary conditions, as described below.

For subsonic inflow, there is only one outgoing characteristic and two physical boundary conditions must be specified. Thus, we impose constant mass flux and constant entropy conditions at the duct inlet:

$$d(\rho u)\,\big|_{x=0} = 0 \quad \Rightarrow \quad d\big[\ln(\rho u)\big]\,\big|_{x=0} = d\big[\ln(\rho)+\ln(u)\big]\,\big|_{x=0} = 0 \tag{65}$$

and

$$d\left(p/\rho^{\gamma}\right)\,\big|_{x=0} = 0 \quad \Rightarrow \quad d\left[\ln\left(p/\rho^{\gamma}\right)\right]\,\big|_{x=0} = d\big[\ln(p)-\gamma\ln(\rho)\big]\,\big|_{x=0} = 0 \ , \tag{66}$$

from which we deduce the following differential relationships and their equivalent linearized acoustic forms:

$$\frac{du}{u} = -\frac{d\rho}{\rho} \Rightarrow \frac{u'}{\bar{u}} = -\frac{\rho'}{\bar{\rho}} \tag{67}$$

and

$$\frac{dp}{p} = \gamma\frac{d\rho}{\rho} \Rightarrow \frac{p'}{\bar{p}} = \gamma\frac{\rho'}{\bar{\rho}} \ . \tag{68}$$

Note that equation (68) applies not only at the inlet but throughout the duct since entropy must remain invariant along the entire flow path as previously deduced as a consequence of equations (49)–(51). Combining equations (67) and (68) yields an expression defining the impedance function at the duct inlet,

$$\left.\frac{p'}{\bar{p}}\right|_{x=0} = -\gamma\left.\frac{u'}{\bar{u}}\right|_{x=0} \Rightarrow z_{in} = -\gamma \ . \tag{69}$$

For subsonic outflow, there are two outgoing characteristics and it is only necessary to specify one physical boundary condition. In this case, we introduce an acoustical admittance condition for mass flux at the duct exit:

$$\left.\frac{\rho u'}{\bar{\rho}\bar{u}}\right|_{x=l_d} = a\left.\frac{p'}{\bar{p}}\right|_{x=l_d} \ , \tag{70}$$

from which we deduce the following differential relationship and its equivalent linearized acoustic form:

$$\frac{du}{u} + \frac{d\rho}{\rho} = a\frac{dp}{p} \Rightarrow \frac{u'}{\bar{u}} + \frac{\rho'}{\bar{\rho}} = a\frac{p'}{\bar{p}} \quad . \tag{71}$$

Eliminating $\rho'/\bar{\rho}$ using equation (68), which applies throughout the duct, yields an expression defining the impedance function at the duct exit:

$$\left.\frac{p'}{\bar{p}}\right|_{x=l_d} = -\frac{\gamma}{1-\gamma a}\left.\frac{u'}{\bar{u}}\right|_{x=l_d} \Rightarrow \quad z_{ex} = -\frac{\gamma}{1-\gamma a} \quad . \tag{72}$$

The working relation for the acoustic amplification coefficient follows from elimination of the inflow and outflow impedances in equation (63) using the results of equations (69) and (72).

3.2 Evaluation of Numerical Methodology

The numerical methodology is evaluated and validated by comparing CFD predictions with small disturbance linear acoustics theory for unsteady, isentropic duct flow. Here, a small amplitude first-mode pressure perturbation is imposed on the computed mean duct flow, and the computation is restarted to observe the temporal evolution of this acoustical disturbance for a given outflow admittance coefficient. By arbitrarily specifying the exit-plane admittance coefficient, it is possible to obtain growing or decaying acoustic waves as desired. The resulting stability attributes, as defined by the amplification coefficient and period of oscillation, may then be directly compared with linear acoustics theory. For simplicity, the physical properties of air were utilized for all calculations. The physical conditions for the baseline duct acoustics problem were $l_d = 0.5$ m, $\bar{M} = 0.2$, $\bar{p} = 1$ atm, and $\bar{T} = 300$ K.

A series of computations were first carried out to examine the influence of grid density on numerical performance. These calculations were based on a fixed exit plane admittance value, a=–0.1, for which small-disturbance linear acoustics theory predicts λ=19.56 s^{-1} and P = 3.00 ms (i.e., f = 333 Hz) for the fundamental mode. The relatively large value for λ implies rapidly increasing acoustic wave strength culminating in the development of large amplitude acoustic shocks. The numerical calculations were performed with 50, 100, 150, and 200 grid points using EI and CN time integration with the convective fluxes evaluated using 2CD, 2UP, and 3UP schemes. The temporal evolution of pressure at the outflow boundary was then used to compute the amplification coefficient and oscillation period during the early growth period when the acoustic amplitudes were small. The results are summarized in tables 1 and 2.

Inspection of these tabulations reveals that the grid density has a strong effect on the predicted amplification coefficient but an extremely weak effect on the oscillation period. It is also evident that the first-order EI technique yields poor stability predictions, irrespective of flux differencing scheme, and even results in wave decay for grossly coarse grids. The second-order CN scheme, on the other hand, performs much better. Although it slightly under predicts wave growth rate, the method is probably adequate for determining approximate stability limits. The best all-around results were obtained when using CN time integration with an upwind flux differencing scheme.

Table 1. Computed amplification coefficient, λ (1/s). (Linear theory: $a = -0.1$, $\lambda_{linear} = 19.56\ s^{-1}$, and $P_{linear} = 3$ ms.)

N_{grid}	EI/2CD	EI/2UP	EI/3UP	CN/2CD	CN/2UP	CN/3UP
50	–38	–40	–40	12.5	10	10
100	–7.1	–9.2	–9.1	14.3	15.1	15.1
150	1.8	1.3	1.3	14.8	15.9	15.9
200	6.3	6.1	6	15.6	16.4	16.4

Table 2. Computed oscillation period, P (ms). (Linear theory: $a = -0.1$, $\lambda_{linear} = 19.56\ s^{-1}$, and $P_{linear} = 3$ ms.)

N_{grid}	EI/2CD	EI/2UP	EI/3UP	CN/2CD	CN/2UP	CN/3UP
50	2.98	2.98	2.98	2.92	2.98	2.98
100	2.99	2.99	2.99	2.98	2.99	2.99
150	2.99	2.99	2.99	2.99	2.99	2.99
200	2.99	2.99	2.99	2.99	2.99	2.99

Comparison of small disturbance linear acoustic theory with the CN/upwind differencing CFD method indicates the need for a minimum grid density to obtain reliable predictions. In general, this can be expressed as a minimum number of grid points per wavelength for the fundamental longitudinal mode:

$$N_\lambda = \frac{N_{grid}}{2l_d} \geq 100 \ \text{ nodes/wavelength} \ . \tag{73}$$

As an example, figure 3 shows the predicted pressure fluctuations at the duct exit for a 200-grid-point CFD calculation superimposed with the amplitude envelope from small disturbance linear acoustic theory. To better illustrate the comparison, figure 4 presents the same data over a smaller time interval with the corresponding power spectrum inset. Here, the CFD results closely follow the classical exponential growth rate predicted by linear theory until the oscillations become large enough to induce significant nonlinear effects. Beyond this point, the wave front gradually steepens into an acoustic shock as the amplitude growth rate declines and a limit cycle oscillation is established. This example also serves to illustrate the nonoscillatory, high-resolution features of the numerical scheme.

As further validation, it is of interest to examine the CFD predicted amplification coefficient as a function of the outflow admittance coefficient in comparison to linear acoustic theory. These results are shown in figure 5 over a relevant range of admittance values. In general, the CFD methodology slightly

under predicts the wave amplification rate over the full range of admittance values. This behavior is more pronounced when the admittance magnitudes become large and nonlinear mechanisms have an appreciable effect. Because the CFD predicted instability growth rates err on the conservative side, it is believed that the method is sufficiently accurate for studying alternative combustion models and their resulting impact on system stability.

4. APPLICATION

Some sample combustor stability calculations are now examined for illustrative purposes. The representative results are intended to provide concrete utilization examples and demonstrate how combustion models may be used to study instability characteristics. The first step in evaluating combustor stability characteristics is to compute a mean flow solution using the two-zone combustion model with all sensitivity indices set to zero. This also requires specification of the mean chamber pressure at the nozzle entrance. Once a fully converged steady-state solution has been obtained, the calculation may be restarted using nonzero combustion response indices. In this case, the short-nozzle admittance approximation is invoked for the outflow boundary condition. From a practical perspective, rocket combustor instabilities arise from broadband disturbances in the chamber, and each mode will grow or decay according to its own response attributes. Here, the initial disturbance is simply provided by a pressure perturbation of the first longitudinal-mode oscillation.

4.1 Generic Rocket Chamber

For the example calculations, representative physical conditions and propellant properties were specified for a generic liquid-propellant rocket engine. The geometric dimensions for this generic rocket chamber were $l_c = 0.5$ m and $A_{in} = A_{ex} = 0.05$ m^2, and the chamber conditions were $\bar{p}_{ex} = 34$ atm, $T_{\text{flame}} = 2,800$ K, and $\dot{m}_{tot} = 50$ kg/s. The thermodynamic properties of the burned propellant were taken to be $\gamma = 1.2$ and $C_p = 1,800$ m^2/s$^2 \cdot$K. All calculations were performed on a 100-grid-point mesh using the CN/2UP algorithm.

Two distinct cases were examined using the two-zone combustion model. Case I assumed that the entire combustion process was collapsed on the injector face such that all propellant entered the chamber in gaseous form at a mean temperature corresponding to the specified flame temperature, $\bar{T}_s = T_{\text{flame}} = 2,800$ K. The mean transpiration Mach number at the inflow boundary was therefore adjusted to obtain the proper total mass flow rate of the rocket (i.e., $\bar{M}_s = 0.243$). Case II assumed one-fifth of the propellant was reacted in a collapsed combustion zone at the injector face while the remainder was injected as a well-dispersed spray with zero atomization length. In this case, the mean transpiration temperature and Mach number were taken to be $\bar{T}_s = 1,000$ K and $\bar{M}_s = 0.03$, respectively. The spray droplets had an SMD of 100 μm, a density of 750 kg/m^3, and entered the chamber with a velocity of 75 m/s. Upon injection, the physical droplets were grouped into numerical parcels represented by a uniform spatial distribution with a half-width equal to the computational grid spacing. The temporal behavior of the entire collection of physical droplets was then determined from the history of a single droplet as it was transported and reacted according to the distributed combustion model, assuming a mean droplet burn rate of 1 mm^2/s.

4.2 Stability Limits

4.2.1 Case I—Fully Collapsed Combustion

Because the entire combustion process is fully collapsed onto the injector face for case I conditions, the burned gas simply enters the chamber at the specified flame temperature with a velocity that satisfies mass conservation. The absence of distributed combustion leads to a trivial mean flow solution through the chamber. The stability characteristics of the combustor were then examined by invoking the short-nozzle admittance approximation and restarting the calculation from the mean flow solution with a 1-percent initial pressure disturbance to the first longitudinal-mode oscillation. The mass transpiration rate of the collapsed combustion zone was made sensitive to pressure fluctuations by imposing nontrivial combustion response attributes using the two-parameter phenomenological model defined in equation (30).

For demonstration purposes, we arbitrarily set $\beta_s = 0$ and varried α_s to determine system stability limits. When $\alpha_s = 0.9$, for instance, the combustor exhibited a stable response to the imposed disturbance, as illustrated in the decaying pressure waveform of figure 6. However, if the combustion response index was slightly increased, such that $\alpha_s = 1$, the combustor became unstable and the pressure wave amplitude was found to grow, as shown in figure 7. As the combustion response index became even larger, the amplification rate continued to increase as illustrated for $\alpha_s = 1.1$ and $\alpha_s = 1.2$ in Figures 8 and 9, respectively. The resulting Case I combustor stability characteristics are summarize in figure 10, which shows the predicted amplification coefficient as a function of the pressure-sensitive combustion response index, α_s. The stability limit for this particular case is $\alpha_s \approx 0.95$.

4.2.2 Case II—Partially Collapsed Combustion

For case II conditions, the combustion process is partially collapsed onto the injector face with 20 percent of the total mass flow entering the chamber through a transpiring reactive boundary. The remaining 80 percent of the propellant is injected as a spray and consumed according to the distributed combustion model. The converged mean mass flow and Mach number distributions for case II conditions are shown in figure 11. Again, stability characteristics of the combustor were examined by invoking the short-nozzle admittance approximation and restarting the calculation from the mean flow solution with a 1-percent initial pressure disturbance to the first longitudinal-mode oscillation. The difference from case I being that the mass transpiration rate of the collapsed combustion zone was made insensitive to pressure fluctuations (i.e., $\alpha_s = \beta_s = 0$) whereas the distributed combustion process was made sensitive to pressure and velocity fluctuations by imposing nontrivial combustion response attributes using the two-parameter phenomenological model defined in equation (40).

For demonstration purposes,we arbitrarily set $\beta_v = 0$ and varried α_v to determine system stability limits, assuming zero phase lags ($\tau_\alpha = \tau_\beta = 0$). Figure 12 shows the unstable response of the combustor to the initial disturbance when $\alpha_v = 1$. Here, combustion pressure coupling was strong enough to overcome damping effects and acoustic nozzle losses to drive instability. The pressure wave amplitude was observed to grow exponentially until nonlinear effects lead to the formation of a limit cycle oscillation with a peak fluctuation >10 percent of the mean pressure. The resulting limit cycle oscillation is periodic but not perfectly sinusoidal with nonlinearities clearly evident in the waveform. This observation is reinforced by the spatial pressure profiles within the unstable combustor, as shown in figure 13 at various time

intervals, where the pressure wave is impinging the injector face and being reflected back toward the nozzle. The resulting case II combustor stability characteristics are summarize in figure 14, which shows both the predicted amplification coefficient and the limit cycle peak-to-peak pressure fluctuation as a function of the pressure-sensitive combustion response index, α_v. The stability limit for this particular case is $\alpha_v \approx 0.7$.

5. CONCLUSIONS

A computational method was developed for the analysis of longitudinal-mode liquid-propellant rocket combustion instability based on the unsteady, quasi-one-dimensional Euler equations with appropriate source terms. These equations were integrated in time using second-order, high-resolution, characteristic-based, flux differencing spatial discretization with Roe averaging of the Jacobian matrix. A two-zone combustion model was introduced where the propellant is either reacted in a collapsed combustion at the injector face or in a distributed combustion process with interphase transport derived from a Lagrangian treatment of representative spray droplets. The local combustion rate was made sensitive to pressure and velocity fluctuations through the simple introduction of proportional combustion response indices. It was also necessary to properly implement reflectance/admittance boundary conditions for impinging acoustic waves in such a way that damping mechanisms would be accurately represented.

For baseline validation, it was convenient to compare CFD predicted wave amplification rate and oscillation frequency with small disturbance linear acoustics theory for unsteady, nonreacting, isentropic duct flow. The major findings of that validation effort were as follows: (1) The best all around CFD performance was obtained when using CN time integration with an upwind flux differencing scheme and (2) reliable CFD predictions could only be obtained when the computational mesh exceeded a minimum grid density per wavelength, $N_\lambda = 100$. Although the second-order CN scheme under predicts wave growth rate to a slight degree, the method is generally adequate for determining system stability limits based on available combustion process models.

Although the current development has been confined to an over-simplified linear combustion response model, more comprehensive physical submodeling can be readily implemented as desired by the analyst. In fact, it appears that the most important use of CFD tools for rocket combustion instability is to serve as a research test-bed for investigating the effect of alternative physical submodels on underlying processes. For illustrative purposes, some sample stability calculations were carried out for a generic combustor configuration. The objectives of this basic exercise were to demonstrate computer code utilization procedures for instability calculations and investigate the effect of our simplified collapsed and distributed combustion process models on instability characteristics. Using this approach, it was shown how the computational methodology could be used to directly determine linear stability limits as well as reveal important nonlinear effects—particularly as they relate to the development of steep fronted acoustic waves and long-term limit cycle oscillations.

In conjunction with experimental data, much could be learned about the chemico-physical nature of combustion driven instabilities through CFD analyses. With time, as modeling becomes more refined through interplay between experiment, theory, and computation, it should be possible to evolve a predictive capability that would directly aid and support engine design and development activities. It is hoped that the computational framework developed herein will serve as a meaningful contribution towards that goal. Beyond submodel refinements and essential validation efforts, the next logical evolutionary step

would be to extend the framework to multiple dimensions for inclusion of tangential-mode instabilities, which are known to play a central role in the most dangerous and destructive forms of liquid-propellant rocket resonant combustion.

REFERENCES

1. Yang, V.; and Anderson, W. (eds.): *Liquid Rocket Engine Combustion Instability (Progress in Astronautics and Aeronautics)*,Vol. 169, AIAA, Washington, DC, 1995.

2. Hsieh, K.C.: "Assessment of Numerical Techniques for Unsteady Flow Calculations," AIAA Paper 89–1956, 1989.

3. Roe, P.L.: "Approximate Riemann Solvers, Parameter Vectors, and Difference Schemes," *J. Computational Phys.,* Vol. 43, pp. 357–372, 1981.

4. Roe, P.L.: "Characteristics-Based Schemes for the Euler Equations," *Ann. Rev. Fluid Mechanics*, Vol. 18, pp. 337–365, 1986.

5. Harten, A.: "High-Resolution Schemes for Hyperbolic Conservation Laws," *J. Computational Phys*., Vol. 49, pp. 357–393, 1983.

6. Yee, H.C.; Warming, R.F.; and Harten, A.: "Implicit Total Variation Diminishing (TVD) Schemes for Steady-State Calculations," *J. Computational Phys*., Vol. 57, pp. 327–360, 1985.

7. Yee, H.C.: "Construction of Explicit and Implicit Symmetric TVD Schemes and Their Applications," *J. Computational Phys*., Vol. 68, pp. 151–179, 1987.

8. Priem, R.J.: "Roundrobin Calculation of Wave Characteristics in a Fixed Geometry—Operating Conditions Liquid Rocket Using Given Simplified Combustion Equations," procedings of the *JANNAF Workshop on Numerical Methods in Combustion Instability*, Orlando, FL, February 1990.

9. Grenda, J.M.; Venkateswaran, S.; and Merkle, C.L.: "Application of Computational Fluid Dynamics Techniques to Engine Instability Studies," in *Liquid Rocket Engine Combustion Instability (Progress in Astronautics and Aeronautics)*, Yang, V. and Anderson, W. (eds.), Vol. 169, AIAA, Washington, DC, 1995.

10. Crocco, L.; and Sirignano, W.A.: "Effect of the Transverse Velocity Component on the Nonlinear Behavior of Short Nozzles," *AIAA J*., Vol. 4, No. 8, pp. 1428–1430, 1966.

11. Zinn, B.T.: "Longitudinal Mode Acoustic Losses in Short Nozzles," *J. Sound and Vibration*, Vol. 22, No. 1, pp. 93–105, 1972.

12. Morse, P.M.; and Ingard, K.U.: *Theoretical Acoustics*, McGraw-Hill Book Company, New York, p. 701, 1968.

13. Hirsch, C.: *Numerical Computation of Internal and External Flows: Volume 2*: *Computational Methods for Inviscid and Viscous Flow*, John Wiley & Sons, New York, p. 165, 1992.

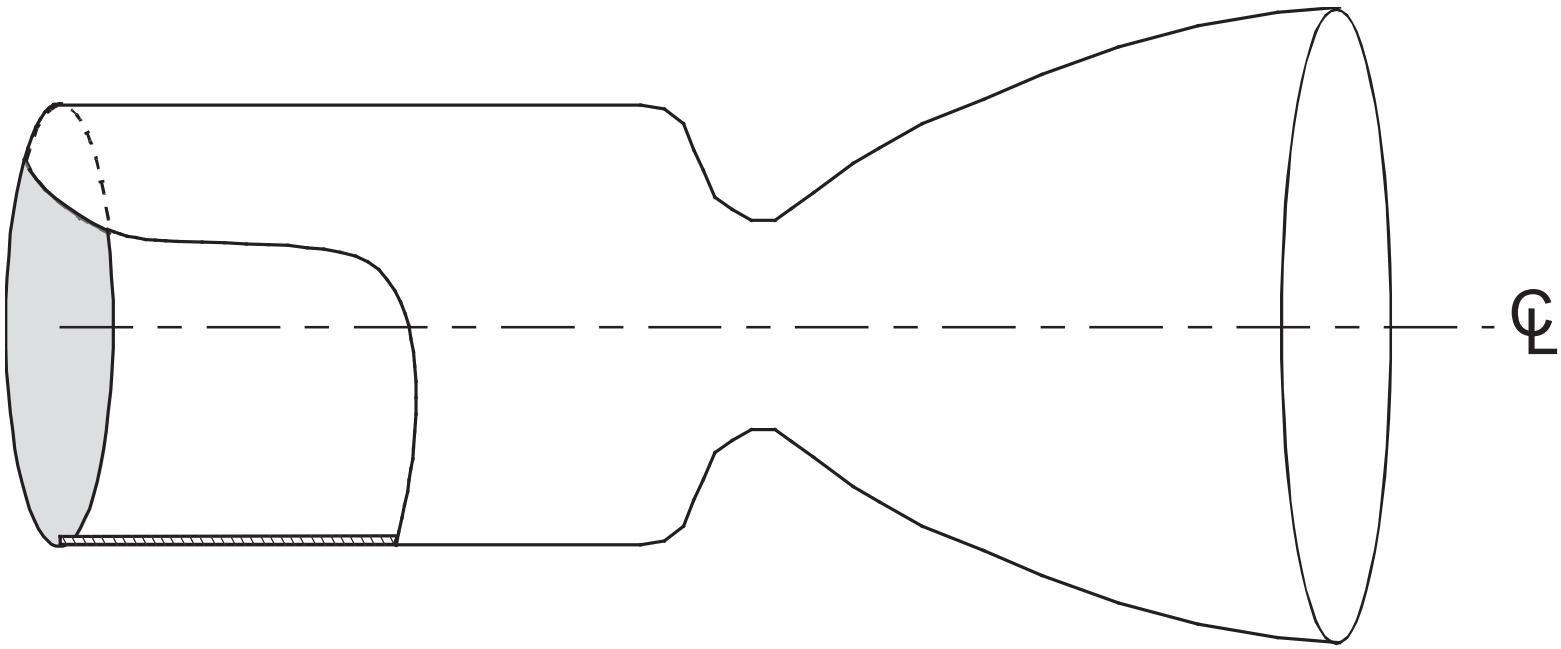

Figure 1. Generalized schematic of a conventional liquid-propellant rocket engine. Liquid propellant enters the chamber through an injector face plate at the head of the engine, and the combusted gases are expanded through a converging-diverging nozzle.

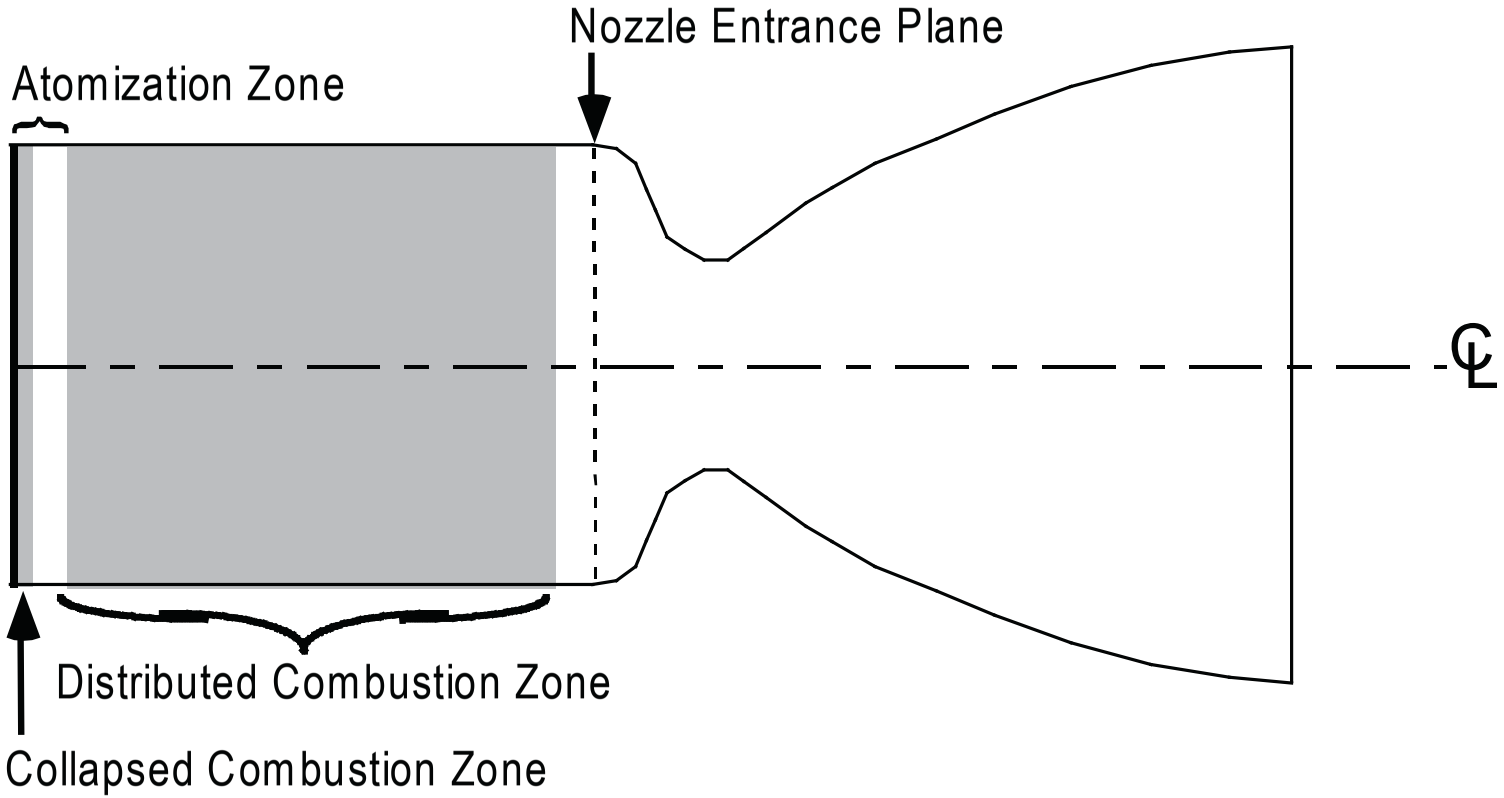

Figure 2. Schematic of computational domain indicating atomization region, collapsed and distributed combustion model zones, and nozzle entrance plane.

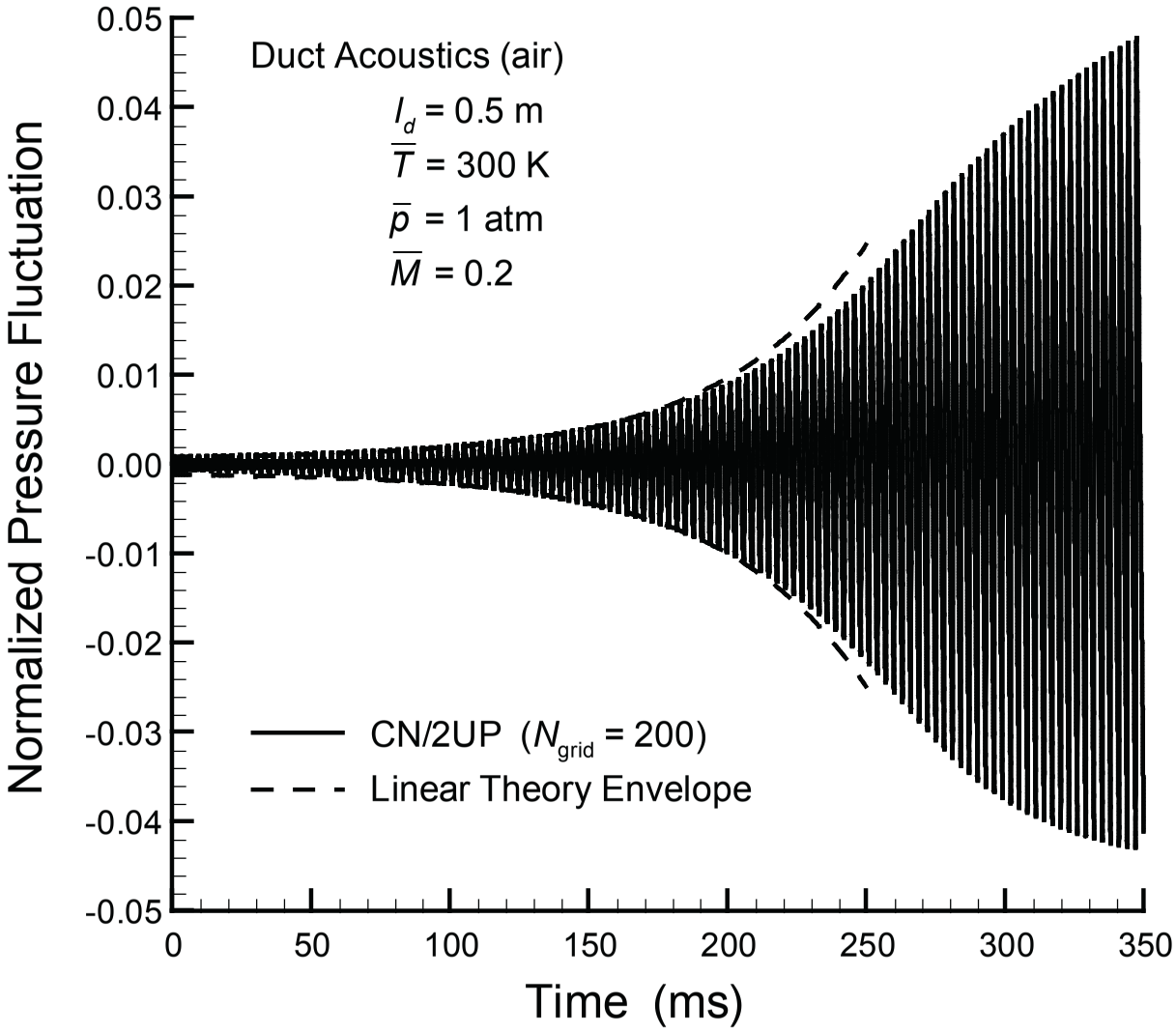

Figure 3. CFD-predicted exit-plane pressure oscillations superimposed with the amplitude envelope from small disturbance linear acoustics theory. Outflow admittance coefficient is $a = -0.1$.

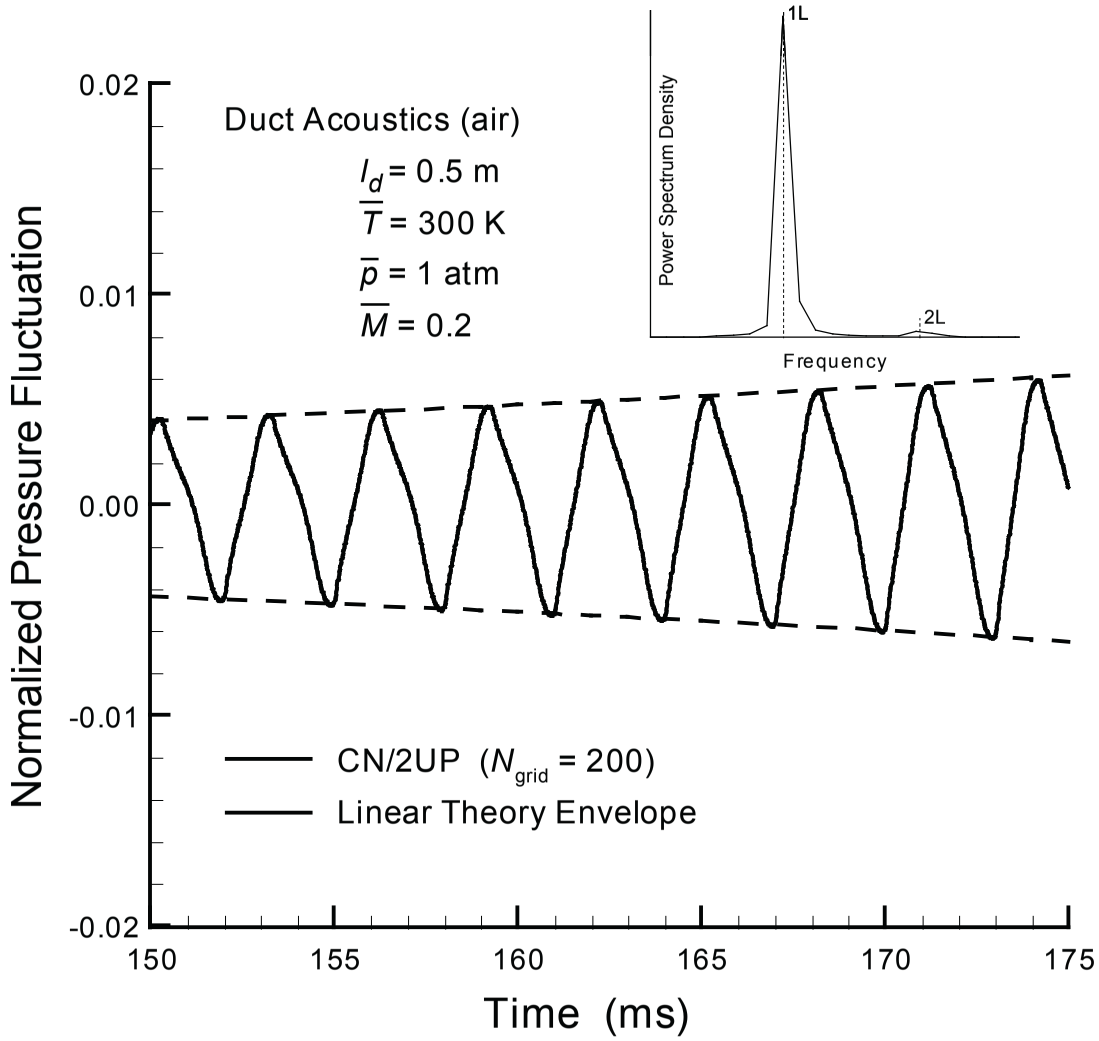

Figure 4. Exploded view of CFD-predicted pressure oscillations superimposed with the amplitude envelope from small-disturbance linear acoustics theory with the corresponding power spectrum inset. Outflow admittance coefficient is $a = -0.1$.

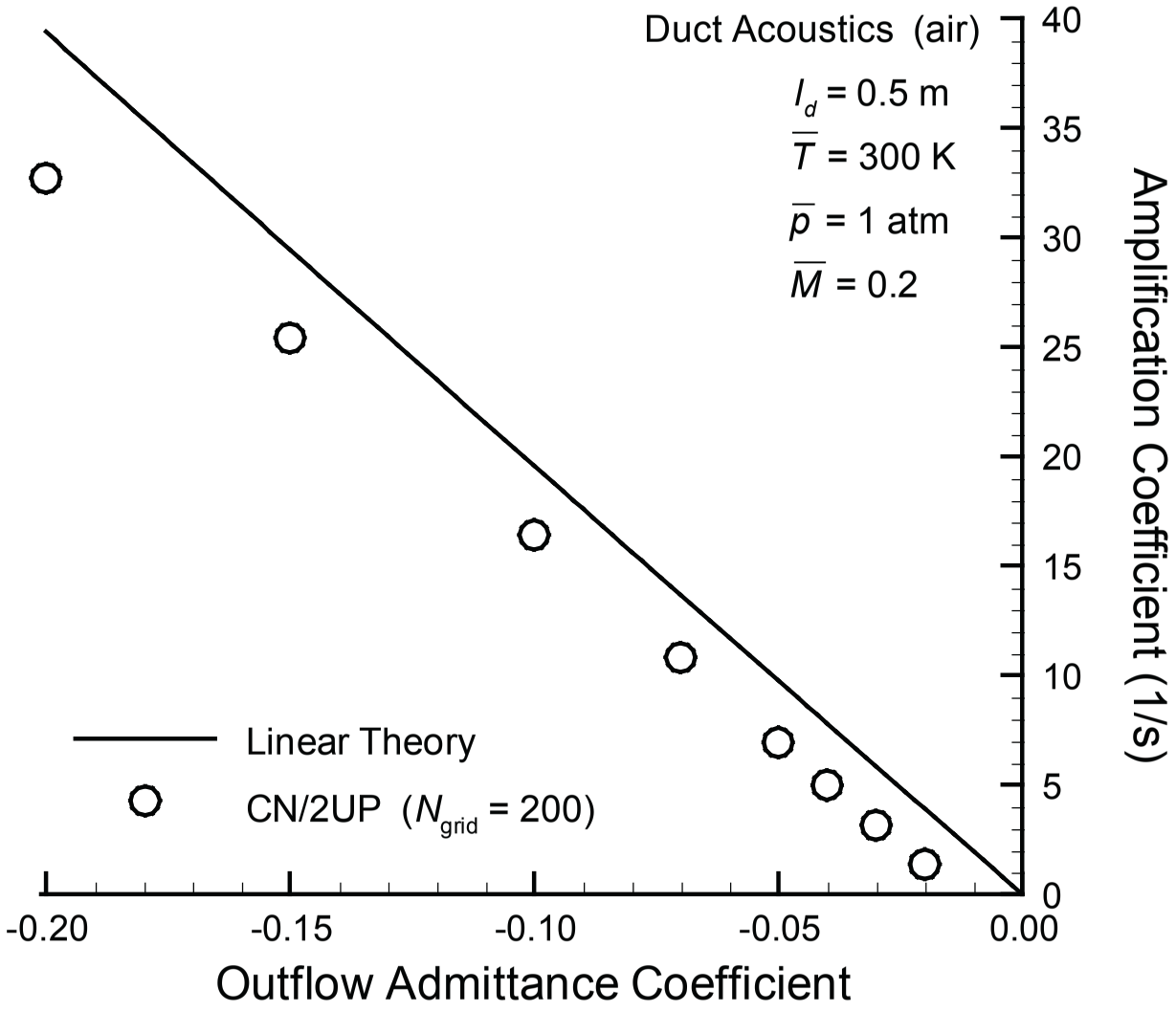

Figure 5. CFD-predicted amplification coefficient as a function of the outflow admittance coefficient in comparison to linear acoustic theory.

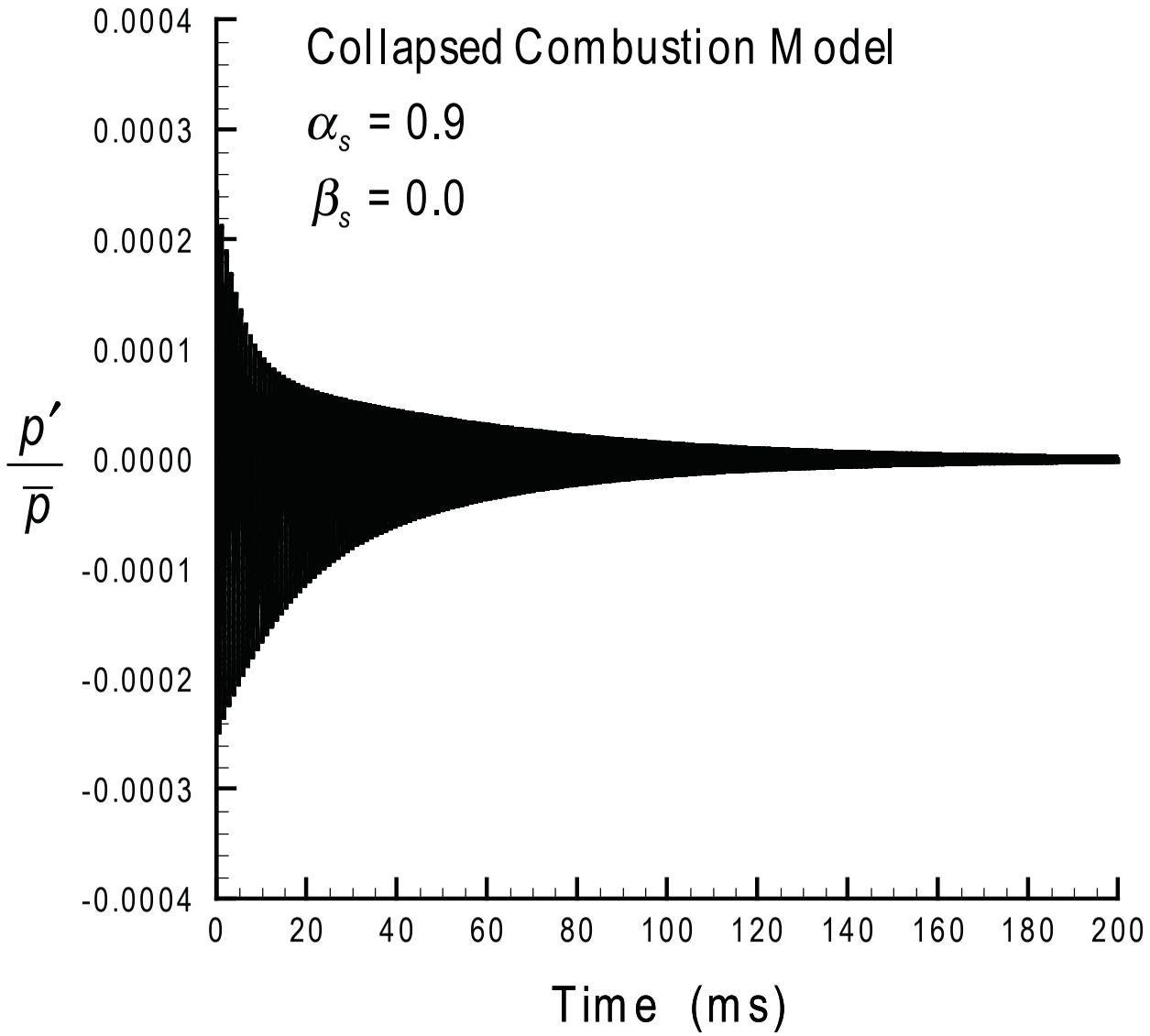

Figure 6. Case I combustor response to 1 percent pressure disturbance with $\alpha_s = 0.9$.

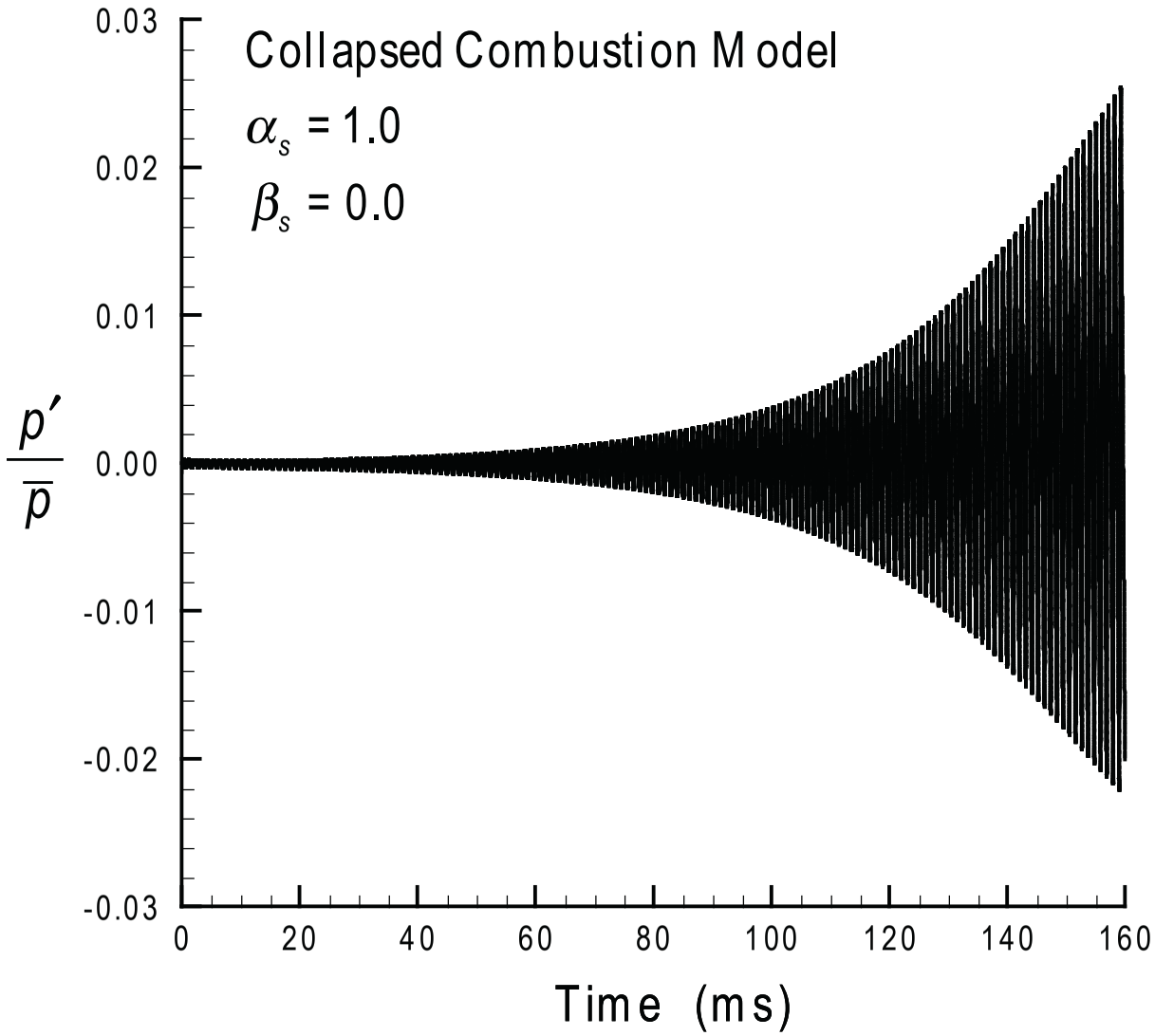

Figure 7. Case I combustor response to 1 percent pressure disturbance with $\alpha_s = 1$.

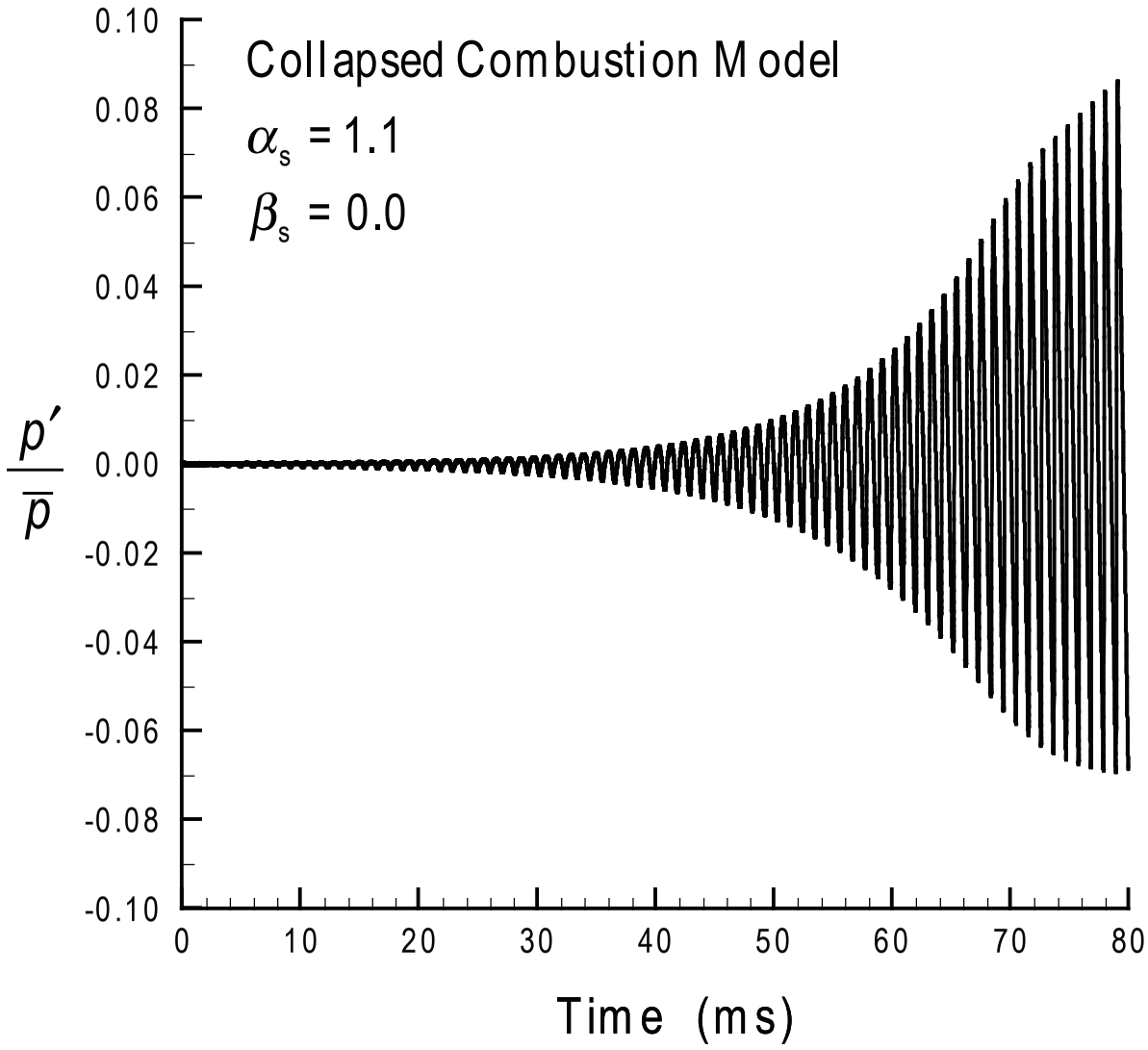

Figure 8. Case I combustor response to 1 percent pressure disturbance with $\alpha_s = 1.1$.

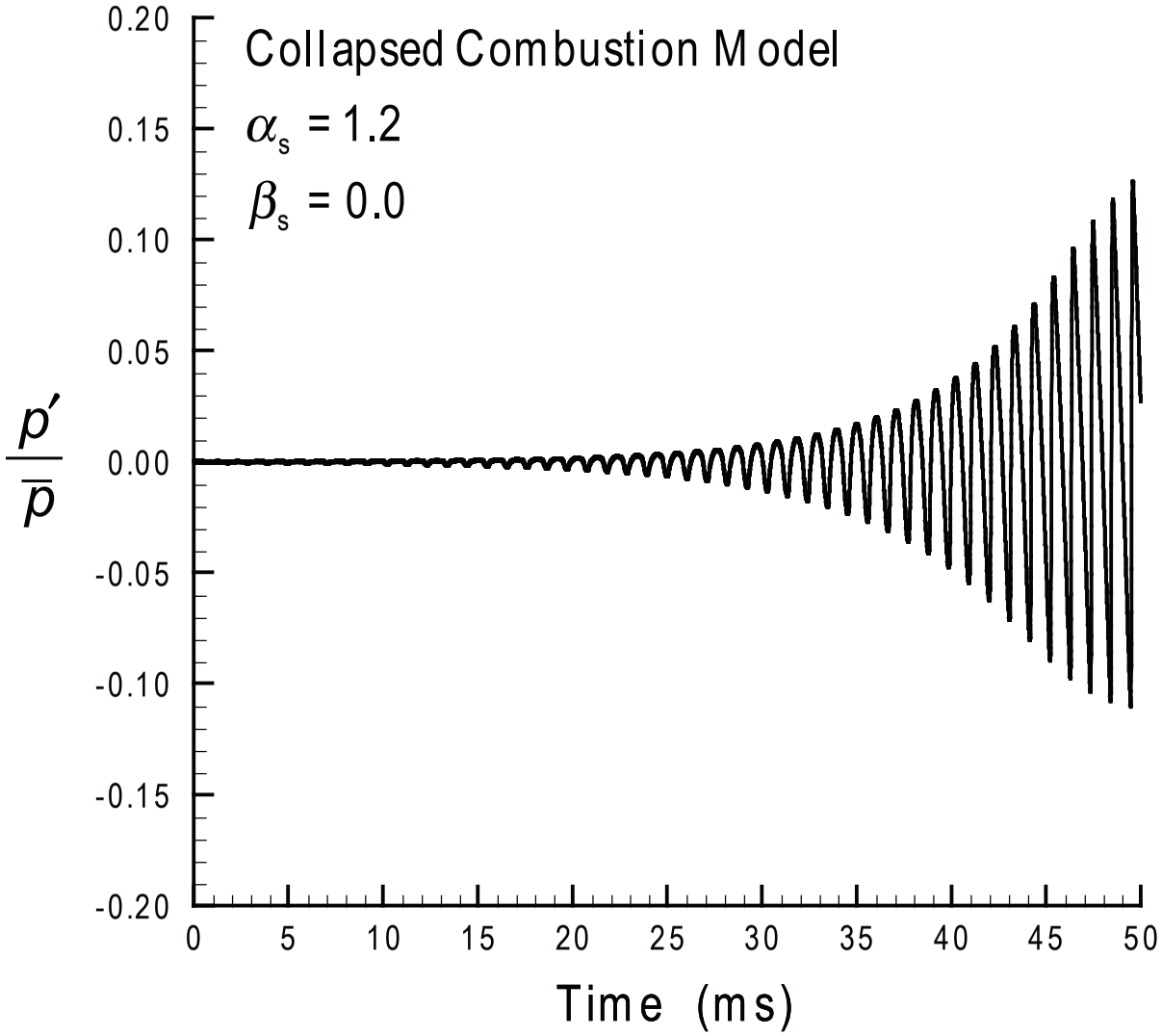

Figure 9. Case I combustor response to 1 percent pressure disturbance with $\alpha_s = 1.2$.

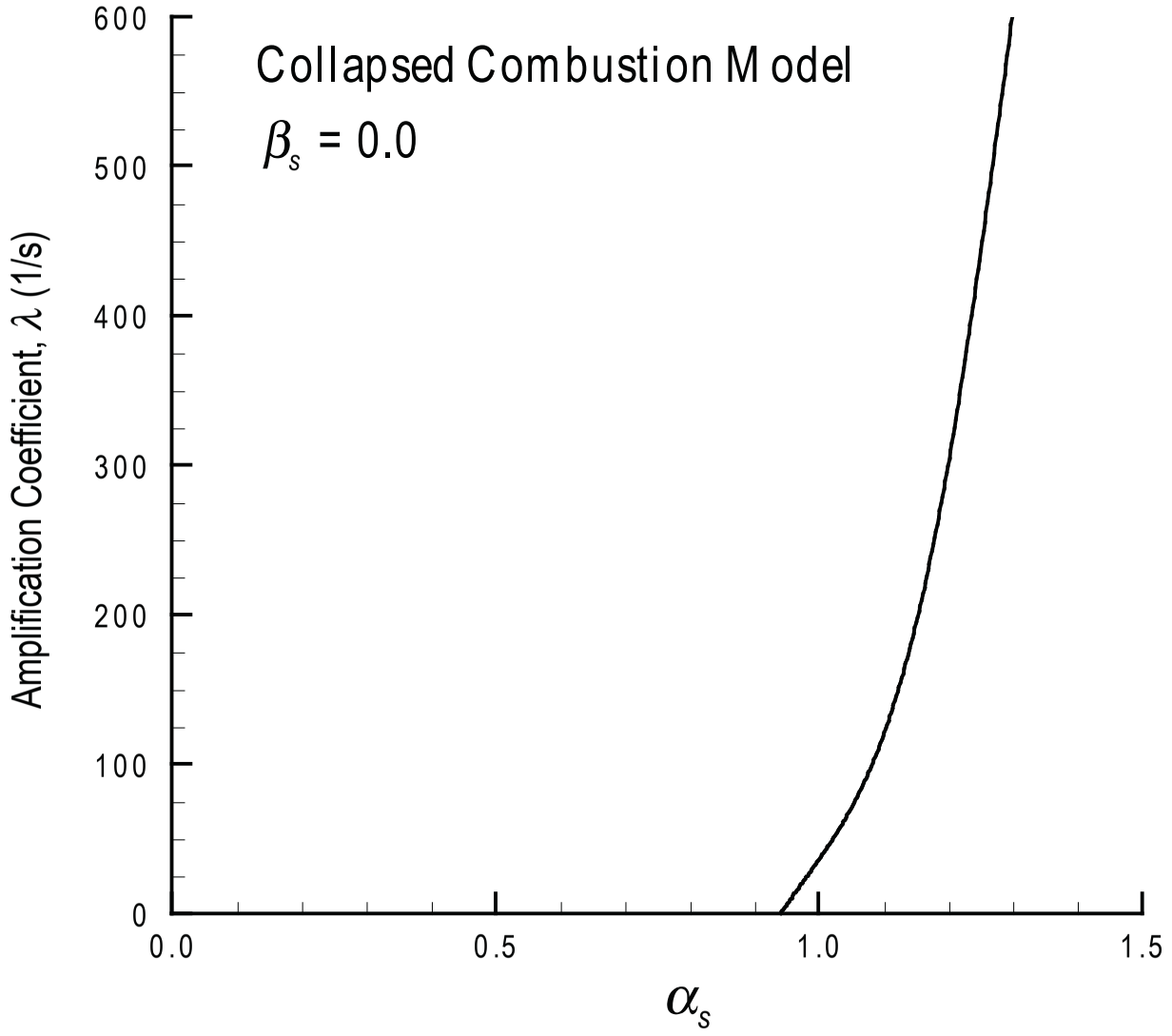

Figure 10. Predicted amplification coefficient as a function of the pressure-sensitive response index for case I conditions.

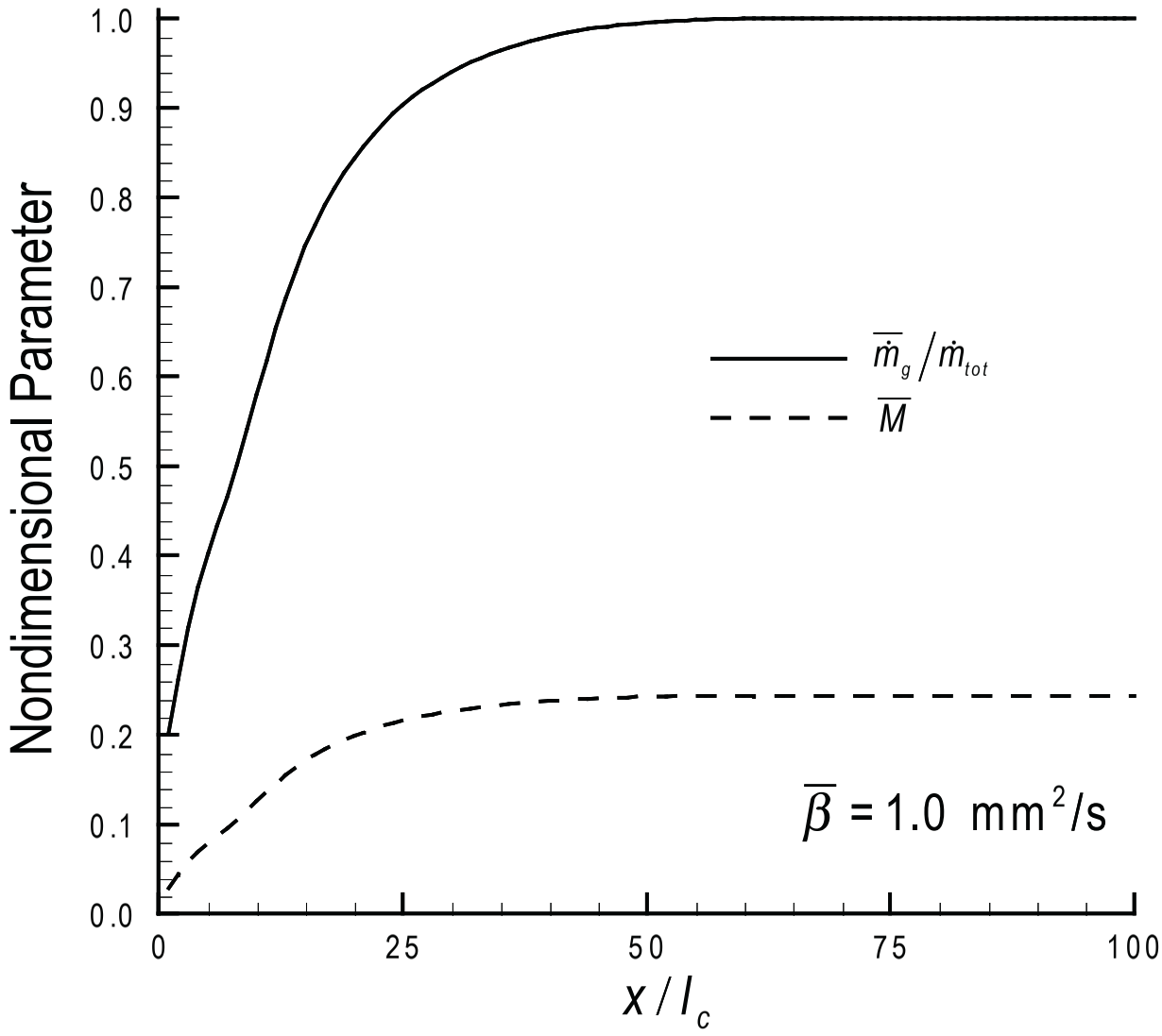

Figure 11. Mean mass flow and Mach number distributions in the combustion chamber for case II conditions.

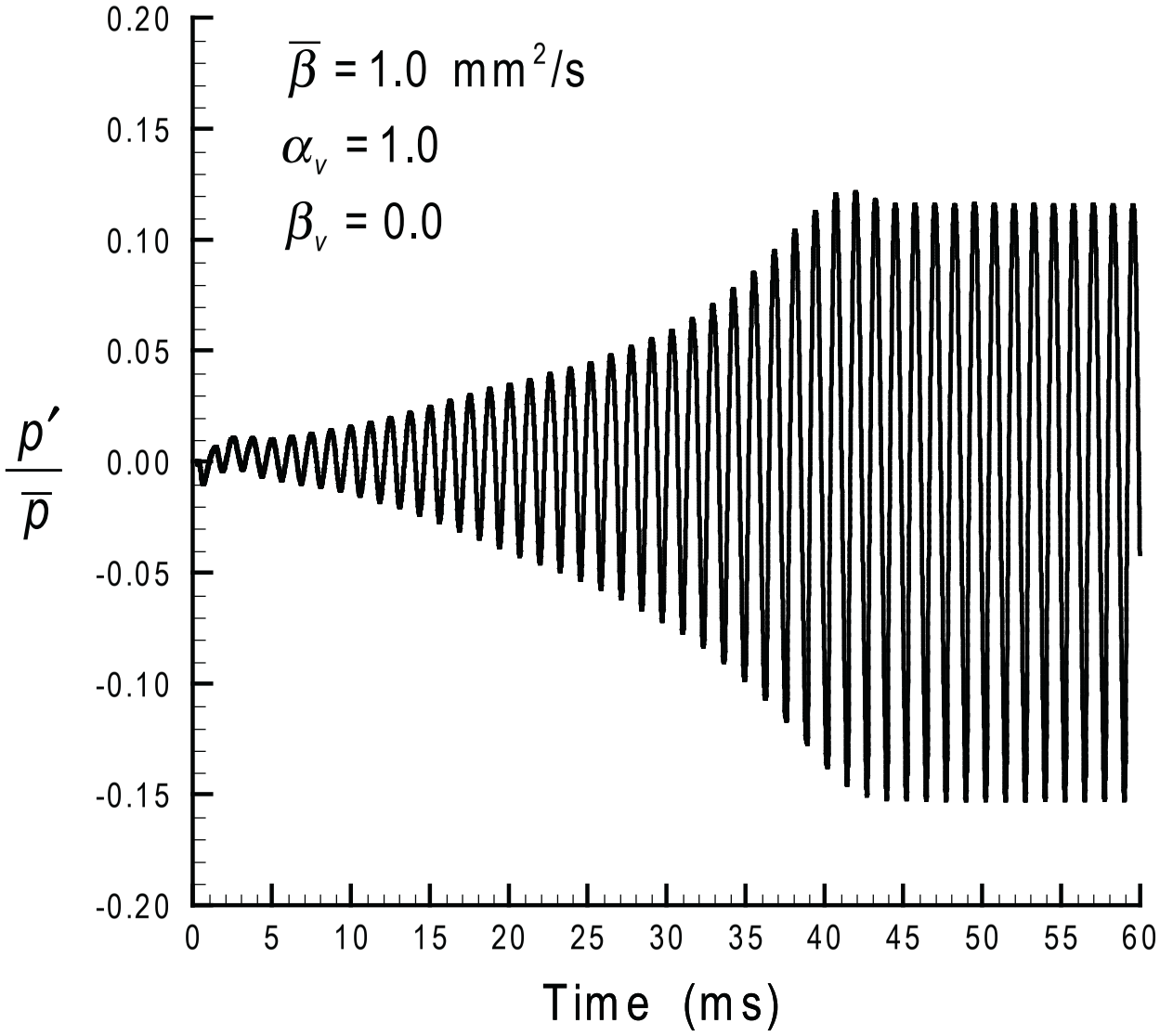

Figure 12. Case II combustor response to 1 percent pressure disturbance with $\alpha_v = 1$.

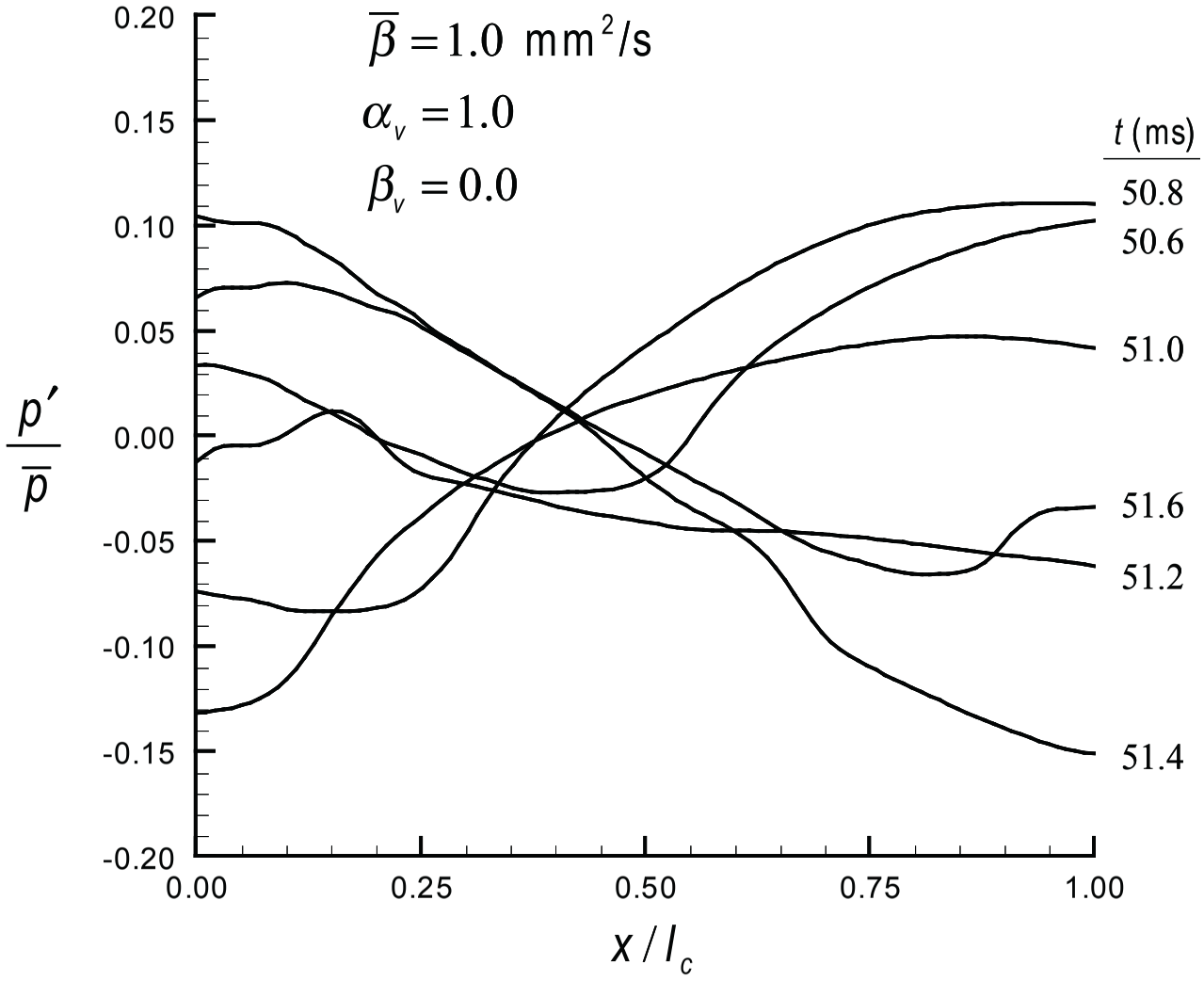

Figure 13. Case II spatial pressure profiles within the unstable combustor ($\alpha_v = 1$) shown at various time intervals.

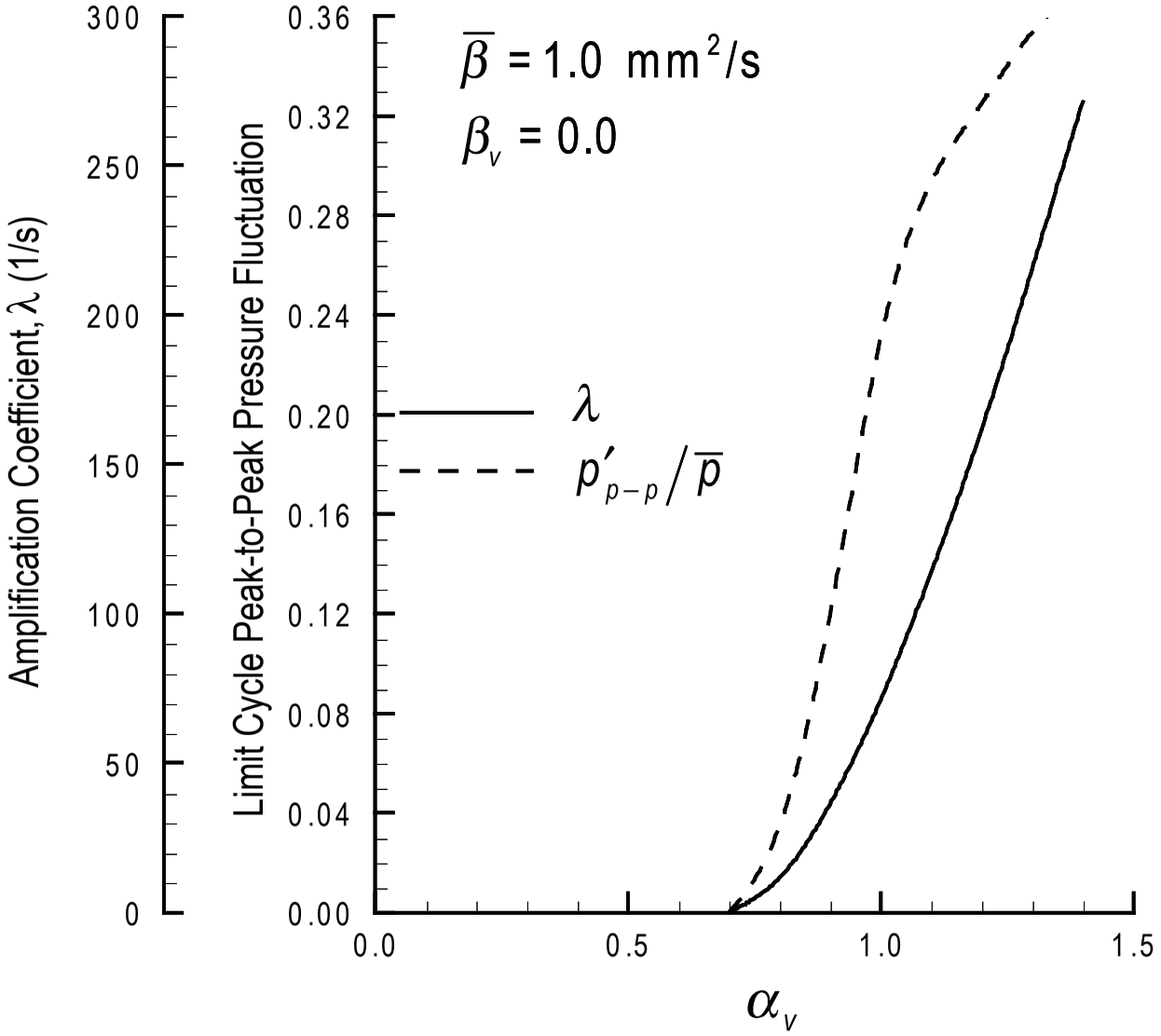

Figure 14. Predicted amplification coefficient and limit cycle peak-to-peak pressure fluctuation as a function of the pressure-sensitive response index for case II conditions.

REPORT DOCUMENTATION PAGE

Form Approved
OMB No. 0704-0188

1. AGENCY USE ONLY *(Leave Blank)*	2. REPORT DATE	3. REPORT TYPE AND DATES COVERED
	September 2005	Technical Publication

4. TITLE AND SUBTITLE

Baseline Computational Fluid Dynamics Methodology for Longitudinal-Mode Liquid-Propellant Rocket Combustion Instability

5. FUNDING NUMBERS

6. AUTHORS

R.J. Litchford

7. PERFORMING ORGANIZATION NAME(S) AND ADDRESS(ES)

George C. Marshall Space Flight Center
Marshall Space Flight Center, AL 35812

8. PERFORMING ORGANIZATION REPORT NUMBER

M–1150

9. SPONSORING/MONITORING AGENCY NAME(S) AND ADDRESS(ES)

National Aeronautics and Space Administration
Washington, DC 20546–0001

10. SPONSORING/MONITORING AGENCY REPO NUMBER

NASA/TP—2005–214188

11. SUPPLEMENTARY NOTES

Prepared by the Propulsion Research Center, Science and Technology Directorate

12a. DISTRIBUTION/AVAILABILITY STATEMENT

Unclassified-Unlimited
Subject Category 20
Availability: NASA CASI 301–621–0390

12b. DISTRIBUTION CODE

13. ABSTRACT *(Maximum 200 words)*

A computational method for the analysis of longitudinal-mode liquid rocket combustion instability has been developed based on the unsteady, quasi-one-dimensional Euler equations where the combustion process source terms were introduced through the incorporation of a two-zone, linearized representation: (1) A two-parameter collapsed combustion zone at the injector face, and (2) a two-parameter distributed combustion zone based on a Lagrangian treatment of the propellant spray. The unsteady Euler equations in inhomogeneous form retain full hyperbolicity and are integrated implicitly in time using second-order, high-resolution, characteristic-based, flux-differencing spatial discretization with Roe-averaging of the Jacobian matrix. This method was initially validated against an analytical solution for nonreacting, isentropic duct acoustics with specified admittances at the inflow and outflow boundaries. For small amplitude perturbations, numerical predictions for the amplification coefficient and oscillation period were found to compare favorably with predictions from linearized small-disturbance theory as long as the grid exceeded a critical density (≈100 nodes/wavelength). The numerical methodology was then exercised on a generic combustor configuration using both collapsed and distributed combustion zone models with a short nozzle admittance approximation for the outflow boundary. In these cases, the response parameters were varied to determine stability limits defining resonant coupling onset.

14. SUBJECT TERMS

liquid-propellant rocket, combustion instability, computational fluid dynamics

15. NUMBER OF PAGES

52

16. PRICE CODE

17. SECURITY CLASSIFICATION OF REPORT	18. SECURITY CLASSIFICATION OF THIS PAGE	19. SECURITY CLASSIFICATION OF ABSTRACT	20. LIMITATION OF ABSTRACT
Unclassified	Unclassified	Unclassified	Unlimited

National Aeronautics and
Space Administration
IS04
George C. Marshall Space Flight Center
Marshall Space Flight Center, Alabama
35812